



# Mapping and characterizing land deformation during 2007–2011 over the Gulf Coast by L-band InSAR

Feifei Qu<sup>a</sup>, Zhong Lu<sup>a,\*</sup>, Jinwoo Kim<sup>a</sup>, Michael J. Turco<sup>b</sup>

<sup>a</sup> Roy M. Huffington Department of Earth Sciences, Southern Methodist University, Dallas, TX 75025, USA

<sup>b</sup> Harris-Galveston Subsidence District, Friendswood, TX 77546, USA

## ARTICLE INFO

Edited by Jing M. Chen

### Keywords:

Gulf Coast

InSAR

Geohazards

Subsidence

Uplift

## ABSTRACT

Land subsidence, known to have occurred in many parts of Gulf Coast of the United States (GC) as a consequence of complex geological conditions, high-intensity resource exploitation and land use. This subsidence has caused extensive damage to buildings and other infrastructures. By exploiting 1650 images from 33 ALOS-1 paths during 2007–2011 using multi-temporal interferometric synthetic aperture (InSAR) techniques, we have constructed, for the first time, a deformation map over 500,000 km<sup>2</sup> of the 1900-km-long GC, with an RMSE of <10 mm/yr. The GC is generally stable, but numerous land deformation zones have been discovered, including at least 30 subsidence patterns and 14 uplift features. The maximum rate of subsidence measured is about 56 mm/yr at Stratton Ridge Oil Field, Texas. Most of the identified ground instabilities are newly discovered as a result of this study. The land deformation along GC is caused by both regional geological conditions and human activities that have influenced natural surroundings and consequentially exacerbated ground instability. Depressurization of petroleum reservoirs and aquifer compaction related to groundwater withdrawal are the principal impactors on observed subsidence. Other processes, including wastewater injection, sulfur/salt mining, dewatering, oxidation, and construction work, also contributed to the InSAR-mapped ground instability. Our large-scale deformation mapping will help the scientific community and relevant agencies better understand land deformation rates and extents, identify the processes responsible for the coastal deformation, and provide a critical dataset for hazard prediction and mitigation in the GC.

## 1. Introduction

Subsidence is a nation-wide problem: approximately 44,000 km<sup>2</sup> in 45 states of the United States have been permanently subsided (Galloway et al., 2008). Land subsidence has caused extensive damage to buildings and other infrastructures (Galloway et al., 1999), changed hydraulic properties of the underground aquifer systems, and resulted in loss of groundwater storage (Fattahi et al., 2017; Jefferson, 1990), reactivated faults (Qu et al., 2019), fissure generation (Qu et al., 2014; Sneed et al., 2003), and through increased seawater intrusion, caused the loss of wetland habitat (DeLaune and White, 2012; Dixon et al., 2006; Fattahi et al., 2017; Galloway et al., 1999; Jones et al., 2014; Jones et al., 2016). The Coastal Lowlands Aquifer System (CLAS) along the GC, covering near 600,000 km<sup>2</sup> of a wide belt from Florida to Mexico (Fig. 1), comprises one of the largest, most complex, and interdependent aquifer systems in the U.S. (Konikow, 2013; Miller, 1999). Historically, groundwater from this aquifer has been the primary source of water for

industrial use, municipal supply, and irrigation in the GC states. Groundwater use in the cities, e.g., Houston and New Orleans, significantly increased to meet the demands of the urbanization and vigorously growing populations for decades, resulting in substantial water-level declines and subsidence (Galloway et al., 1999; Holzer and Galloway, 2005; Konikow, 2013). For example, Greater Houston (GH), Texas is the largest metropolitan region in the U.S. that was affected by land subsidence because of the widespread hydrocarbon withdrawn production and groundwater pumping (Galloway et al., 1999; Holzer and Galloway, 2005). Groundwater pumping has lowered potentiometric water-levels >30 m in Baton Rouge, Lake Charles and southern Mississippi since the urban development started in the early years of the twentieth century as a result of groundwater storage reduction and dehydrated clays compaction (Holzer and Galloway, 2005; Martin and Whiteman, 1999; Morton, 2003; Wintz et al., 1970). Drawdown of ground-water levels has also occurred near New Orleans, Louisiana and the Savannah area in eastern Georgia. However, the oil and/or gas production was the

\* Corresponding author.

E-mail address: [zhonglu@smu.edu](mailto:zhonglu@smu.edu) (Z. Lu).

<https://doi.org/10.1016/j.rse.2022.113342>

Received 4 February 2022; Received in revised form 3 October 2022; Accepted 29 October 2022

Available online 12 November 2022

0034-4257/© 2022 Elsevier Inc. All rights reserved.

primary cause of subsidence over Corpus Christi, Texas (Holzer and Galloway, 2005). A key to protecting life and property is the precise and accurate measurement of subsidence and better understanding of the deformation causes and mechanisms. The complex geologic setting, laterally diverse subsurface hydrological units, regional faults, groundwater and hydrocarbon extraction, and sinkhole development among others in GC have made it difficult to discretely monitor and characterize the land subsidence.

Even though ground-based monitoring techniques, such as GPS, provide high-accuracy subsidence measurements at distinct locations, they have limitations in providing more detailed and comprehensive information on ground deformation. In addition, the operation of ground-based networks in the field is time consuming, labor intensive, and costly, particularly over a large scale. Because the heavy consumption of groundwater under the spatially-variant hydrogeology of the CLAS can induce significant subsidence over extensive areas, temporally and spatially dense observations are required to understand the complicated characteristics underlying the ground deformation, e.g., (Bawden et al., 2012; Coplin and Galloway, 1999; Dixon et al., 2006; Dokka, 2011; Galloway et al., 2008; Galloway et al., 1999; Holzer and Galloway, 2005; Jones et al., 2016; Khan et al., 2014; Konikow, 2015; Martin and Whiteman, 1999; Morton, 2003; Morton et al., 2006; Morton et al., 1983; Qu et al., 2019; Qu et al., 2015; Seifert and Drabek, 2006; Wintz et al., 1970). Interferometric Synthetic Aperture Radar (InSAR) has demonstrated its capability to measure regional or local ground deformation caused by land subsidence, landslides, earthquakes, and volcanoes among others, e.g., (Bawden et al., 2012; Hooper, 2008; Lu and Dzurisin, 2014; Wright et al., 2001). Unlike ground-based measurements, the satellite InSAR technique has the ability to measure deformation within a centimeter- to millimeter-level precision over a

large area. However, InSAR processing and applications over the GC face three main challenges: tropospheric artifacts (regardless of radar frequency), ionospheric anomalies (especially for L-band radars), and decorrelation (over non-urban areas). Because of these shortfalls, InSAR has been applied to only few locations along the GC to study local subsidence over highly-coherent urban areas such as Houston and New Orleans using primarily C-band SAR images, such as ERS and RADARSAT-1, and UAVSAR (Bawden et al., 2012; Buckley et al., 2003; Dixon et al., 2006; Jones et al., 2014; Jones et al., 2016; Khan et al., 2014; Miller and Shirzaei, 2019; Qu et al., 2019; Qu et al., 2015; Stork and Michelle, 2002). The complex coastal environment and limited number of ALOS-1 images make the ALOS-1 data processing over GC difficult. To our knowledge, only a few works have been published over Houston region, (Miller and Shirzaei, 2019; Qu et al., 2019; Qu et al., 2015). Furthermore, few to none studies had previously been conducted for nonurban areas, which occupy >90% of the GC, with substantial amounts of faults, water/oil/gas wells, and distributed salt domes. It is clear that the subsidence in many areas along the GC is incompletely understood and inadequately monitored, and that its threat to safety and economic impact can be severe.

The GC has been exposed to land subsidence/uplift due to its complicated geological constitution and high intensity of land-use. Despite InSAR's capacity of all-weather, day-and-night, broad-coverage, and high-precision monitoring of ground deformation, this space-to-earth observation technology had not previously played a role in quantifying land deformation on a regional scale of the entire GC. The goal of this work is to provide a complete image of land deformation rates and extents over 500,000 km<sup>2</sup> of the 1900-km-long GC, and identify the processes responsible for the coastal deformation using InSAR imagery and auxiliary data source. By employing the MTI

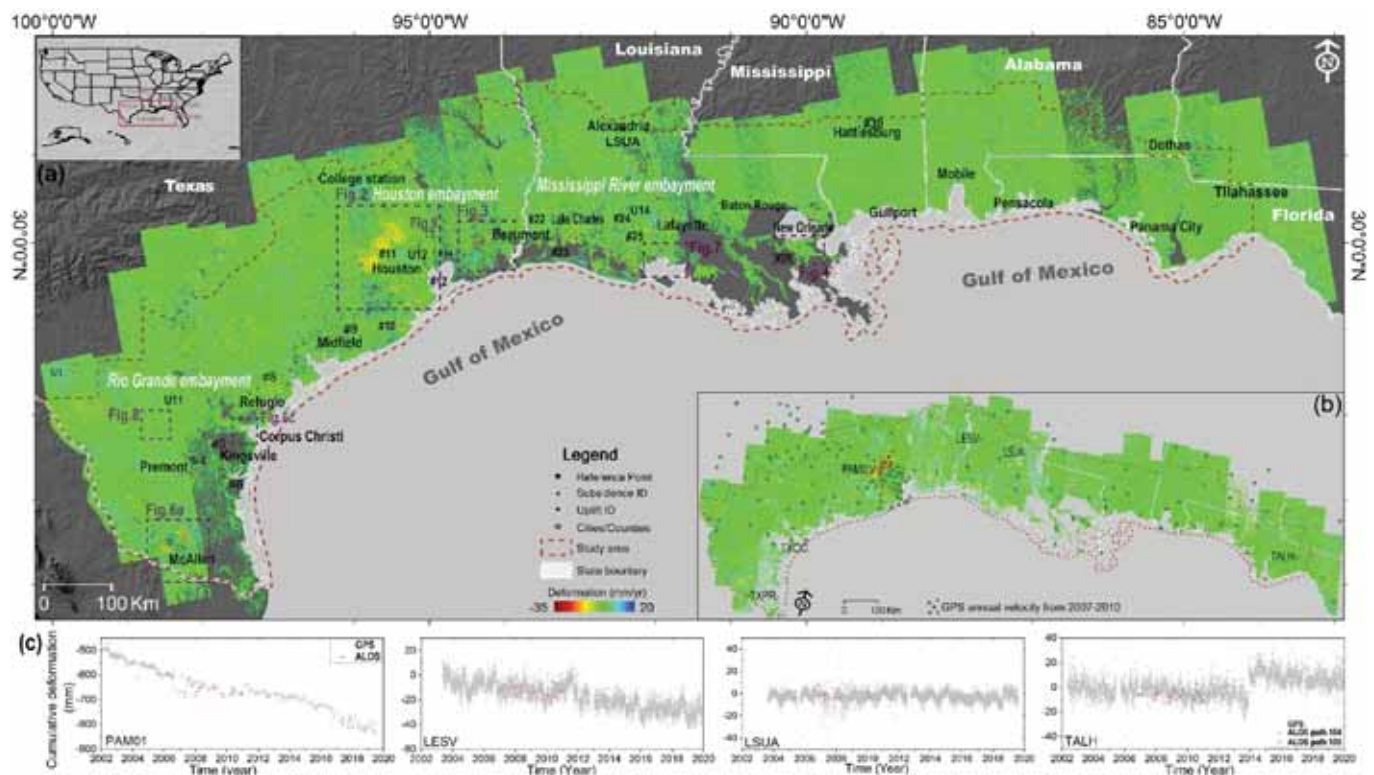


**Fig. 1.** A seamless deformation map over 500,000 km<sup>2</sup> areas of GC: (a) Average vertical deformation map over GC by mosaicking InSAR products from 33 ALOS-1 tracks; (b) Comparison of the average vertical deformation rate between InSAR and GPS measurements during the period of 2007–2011 at stations established after 2009 (Blewitt et al., 2018); (c) Comparison between InSAR-derived time series deformation and GPS observations at 4 stations, whose locations were marked on (b); The “#1 - #30” show the measured subsidence zones and “U1-U14” display the identified uplift features. The dark purple dashed rectangles mark areas that will be discussed in the following main text. The United States map is an inset on the up-left, where the red solid rectangle shows the approximate area of (a). Background: shaded relief map of Gulf Coast.

techniques (Hooper, 2008) and L-band SAR images from ALOS-1 (2007–2011), this work provides, for the first time, a comprehensive analysis about spatial distribution and characteristics of land deformation at a finer spatial resolution over a large span of the GC, discovers many new deformation zones, and highlights each type of major deformation features. This paper is organized as follows: we firstly summarize the data and method used; secondly, we demonstrate InSAR-based observations of surface deformation over GC and exploit GPS measurements to validate and compare with our MTI results; thirdly, we present the main InSAR-measured deformation patterns by five major causes, i.e., groundwater withdrawal, hydrocarbon production, salt mining, wastewater injection and gas storage; finally, we address the land deformation observations and discuss their correlation with the geologic conditions, resource exploitation and land-use changes.

## 2. Methods and data

### 2.1. Method

Satellite InSAR has the ability of surveying ground deformation at a spatial resolution of meters over a wide scale with a centimeter- to millimeter-level accuracy. However, the reliability of conventional InSAR method was limited by spatial and/or temporal decorrelation between SAR acquisitions as well as the orbital and atmospheric phase artifacts (Ferretti et al., 2001; Zebker and Villasenor, 1992). MTI methods, which principally include Persistent Scatterer InSAR (PSInSAR) (Ferretti et al., 2001), and Small Baseline Subset (SBAS) algorithm (Berardino et al., 2002), techniques, overcome the above-mentioned limitations through utilizing series of SAR images. The PS-InSAR method identifies coherent Persistent Scatterer (PS) pixels whose phases remain coherent during the observation interval (Ferretti et al., 2001). We implement the Stanford Method for Persistent Scatterers (StaMPS) for PS-InSAR processing (Hooper, 2008; Hooper et al., 2004; Hooper and Zebker, 2007). PS candidates are initially selected based on amplitude analysis. The PS probability is then estimated by the phase analysis via an iterative process based on the decorrelation noise,  $\gamma_x$ , which represents the variations in the residual between the observed and estimated phases at the PS candidate pixel (Hooper et al., 2004). This method has been successfully applied in urban areas where the resolution elements are primarily dominated by strong reflecting manufactured constructions. The SBAS method selects interferograms whose temporal separations, perpendicular baselines, and Doppler variations are below certain thresholds to maximize interferometric coherence (Berardino et al., 2002; Hooper, 2008). Image pairs are filtered in both range and azimuth to reduce the effects of non-overlapping Doppler spectrum and geometric decorrelation. Slowly-varying filtered phase (SFP) pixels are identified among the candidate pixels in a similar way as for PS pixels. Note that the PS pixels are selected based on single-reference interferograms with no spectral filtering, while SFP pixels are chosen based on multiple-reference small-baseline interferograms with spectral filtering.

The pixels from both PS and SFP are then integrated prior to phase unwrapping (Hooper, 2008). Through combining both PSInSAR and SBAS approaches, MTI can increase the spatial density of usable signal, allowing the identification of PSs that dominate the scattering from the resolution element and SFP pixels whose filtered phases decorrelate little over short time intervals (Hooper, 2008; Qu et al., 2015; Qu et al., 2014). The combined SBAS interferometric phases composed from PS and SFP pixels are then followed by procedures of three-dimensional phase unwrapping and deformation-phase solution. The atmospheric artifact and baseline error are then estimated and eliminated through temporal high-pass filtering and spatial low-pass filtering. The corrected unwrapped phase from selected small baseline interferograms is then inverted to establish time-series phases for all pixels utilizing a least-squares approach. More details about MTI method could be found in (Hooper, 2008).

### 2.2. Datasets and processing

About 1650 of SAR images from 33 ascending L-band ALOS PALSAR tracks have been utilized in this study to illustrate the spatial distributions of land deformation over whole GC. Details about SAR images employed in this work can be found in Table 1. We concatenated sequential single-look-complex (SLC) frames in azimuth direction to create large images in each processing stack. The overlap area of about 10 km in swath between neighboring ALOS tracks was used for validating and mosaicking. In addition, we utilized a  $\sim 30$  m Shuttle Radar Topography Mission (SRTM) DEM as an external DEM to eliminate the topographic phase in generated interferograms. The Doris, ROI-PAC (for ALOS-1) and GAMMA (for ALOS-1/ALOS-2) software are employed for the interferometry processing. Secondary images are registered and resampled to the primary geometry and corrected for the geometry difference between the primary and secondary images using the WGS84 reference ellipsoid. Besides, ionospheric anomalies are present in some interferograms where the split-spectrum method has been applied to mitigate the phase error using Gamma (Wegmüller et al., 2018). The 36 datasets were then processed using the above StaMPS MTI method (both PS and SBAS) respectively (Hooper, 2008). The crucial StaMPS parameters utilized in our MTI processing could be found in Table S1. GACOS (Yu et al., 2018) has been applied to correct tropospheric artifacts in select SAR images, and Toolbox for Reducing Atmospheric InSAR Noise (TRAIN) package (Bekaert et al., 2015) has been implemented to interferograms exhibiting topography-correlated and large-scale components of the tropospheric delay. A deramp processing is also applied to interferograms to eliminate the residual orbital error and long-wavelength atmospheric error. In addition, interferograms that were severely contaminated by high-frequency tropospheric noise were excluded from our processing. Finally, remaining tropospheric artifacts are further estimated and mitigated through temporal high-pass filtering and spatial low-pass filtering. Innocuous turbulent tropospheric delays might still reside in some interferograms due to the limited number of ALOS-1 images in each track.

Ultimately, 36 average line-of-sight (LOS) deformation velocities during 2007 and 2011 were generated utilizing the MTI method. The InSAR-derived velocity maps were visually inspected for residual ramps and also simply compared with the GPS measurements. In several tracks, a flattening processing of the non-deformation area has been applied, because sufficient deformation-free areas are available in each track. In addition, the deformations are transferred into the vertical direction according to the incidence angles to minimize the effects of imaging geometry and assure overlapping areas are compatible in advance of mosaicking. Overall, there was a near universal agreement for both the patterns and rates of deformation between adjacent tracks before mosaicking. To generate a seamless velocity map of GC all stacks were referenced to LASU Continuously Operating Reference Station (CORS) (black star, Fig. 1a), situating at Rapides County, LA, where there was a wealth of high coherence points around and almost no deformation was observed at this station since Aug 31, 2003 (Blewitt et al., 2018). We picked coherent points located within 100-m of the GPS station and averaged InSAR deformation values around it as the InSAR measurement to be rectified. After the reference track was corrected by GPS and all LOS measurements were converted to the vertical displacement, two

**Table 1**  
SAR data characteristics over GC.

Sensor	ALOS-1 PALSAR	ALOS-2 PALSAR-2
Band	L	L
Polarization	HH, HV	HH, HV
Wavelength (cm)	23.6	23.6
Heading (°)	$\sim -10.4$	$\sim -10.1$
Incidence angle (°)	$\sim 38.7$	$\sim 40.6$
Number of used tracks	33	2
Date range (yyyy)	2007–2011	2014–2018



highly coherent patches ( $\sim 200 \times 200$  pixel areas), were selected within the overlapping parts between the reference track and its left and right adjacent tracks as new references to correct the two neighboring tracks respectively. Repeat this step to the other tracks until they were all referenced to the super track. After referencing and correcting for the offset between tracks, we compared the vertical deformation measurements of the overlapped parts from two neighboring displacement maps. Generally, there is a consensus on both the pattern and rate of displacement between neighboring stacks, and the average standard deviation of the 32 differential maps is  $\sim 9$  mm/yr. Combined velocity maps of overlapped areas were created by pixels from both the adjacent tracks, and a weighted mean value for the velocity was calculated by averaging the values from two stacks according to their quality reported by InSAR processing. Although there was no significant inconsistency between adjacent stacks, some minor discrepancies between tracks may occur because of the residual interferometric phase errors and/or the assumption of vertical deformation. Finally, a seamless deformation map over about 500,000 km<sup>2</sup> areas of GC was produced for the first time by mosaicking 33 ALOS tracks (Fig. 1). The deformation mapping processing flowchart is shown in Fig. 2.

### 3. Results

#### 3.1. Average deformation map of Gulf Coast

A seamless deformation map over about 500,000 km<sup>2</sup> areas of the GC during 2007–2011 was produced for the first time by mosaicking 33 70-km-wide ALOS-1 PALSAR tracks (Fig. 1). The GC is generally stable, but

numerous land deformation zones have been realized, including at least 30 subsidence patterns and 14 uplift features (Fig. 1). The maximum rate of subsidence measured is about 56 mm/yr at Stratton Ridge Oil Field in Brazoria County, Texas (Fig. 1). InSAR-derived average deformation observations are compared with velocity measurements from 190 GPS stations coastal-wide (Blewitt et al., 2018). Time-series deformation plots at 4 GPS stations, whose positions can be found in Fig. 1b, are also shown in Fig. 1c. There is a universal agreement between the daily/monthly GPS solutions and the InSAR time-series measurements (Fig. 1c), with an average RMSE (root mean square error) of approximately 10 mm/yr for the difference between vertical deformation measurements from InSAR and GPS.

Ground deformation over the GC is not solely attributed to a single cause, but a combination of several different factors that involve large volumes of extraction of underground reservoirs (water, hydrocarbons, sulfur, and salt) and wastewater injection, as well as processes of sediment compaction, tectonics, and gravity driven process (Galloway et al., 2008; Galloway and Burbey, 2011; Galloway et al., 1999). Our GC-wide observations of ground instability allow us to diagnose the geohazards and the associated mechanisms including groundwater withdrawal, sediment compaction, hydrocarbon production, salt mining, faulting and wastewater injection.

#### 3.2. Land subsidence induced by groundwater withdrawal

Potentiometric surface declines related to large volumes of groundwater withdrawal will cause a reduction in hydraulic pressure in the pores of the granular matrix, resulting in an increased load on the aquifer skeletal matrix. When a growing stress on the skeleton is applied, the unconsolidated or only partially consolidated clay layers might decrease in porosity and then compact, leading to the onset of subsidence (Galloway et al., 1999). Several well-known metropolitan regions in GC affected by heavy groundwater pumping, such as Houston, Baton Rouge, New Orleans, and Lake Charles, have been discussed in previous studies (Galloway et al., 1999; Konikow, 2013, 2015; Qu et al., 2019; Qu et al., 2015; Seifert and Drabek, 2006). We have found some of the published subsidence zones have ceased to be detectable during the period of 2007–2011, while continuing deformation has been observed at the Greater Houston and New Orleans regions by our analysis of ALOS-1 InSAR imagery (Figs. 3 and 5). Our InSAR-derived deformation map has also allowed us to discover one new subsidence feature that may be associated with groundwater withdrawal at Beaumont, TX (Fig. 4). Further results associated with groundwater withdrawal induced subsidence in the Houston, Beaumont and New Orleans areas follow.

##### 3.2.1. Houston, TX

The primary source of the land subsidence in the GH region, comprised of 11 Counties, is attributed to the long-term withdrawal of subsurface fluids, including both groundwater withdrawal and hydrocarbon extraction (Coplin and Galloway, 1999). From 1943 to 1977, water levels declined within the Chicot and Evangeline aquifers, and the consequences of subsidence were generally recorded in central and southeastern Harris County and throughout Galveston County as the groundwater was withdrawn heavily from both aquifers (Coplin and Galloway, 1999). In response, the Harris-Galveston Subsidence District (HGSD) established strict policies governing groundwater withdrawals in Harris and Galveston Counties (Area 1 on Fig. 3a) in 1975, and groundwater drawdown has ceased at all of the wells in Area 1 but continues in west and northwest Harris County, northeastern Fort Bend County, and southern Montgomery County (approximately HGSD Area 3) (HGSD, 2013b). As a result, we have measured a slight rise in land-surface elevation over HGSD Area 1 after 2000. In contrast, groundwater withdrawals were not restricted until 2010 in Area 3 (HGSD, 2013a), resulting in a continuous decline in water levels in the aquifers and land subsidence of about 20 mm/yr (Fig. 3). InSAR and GPS data

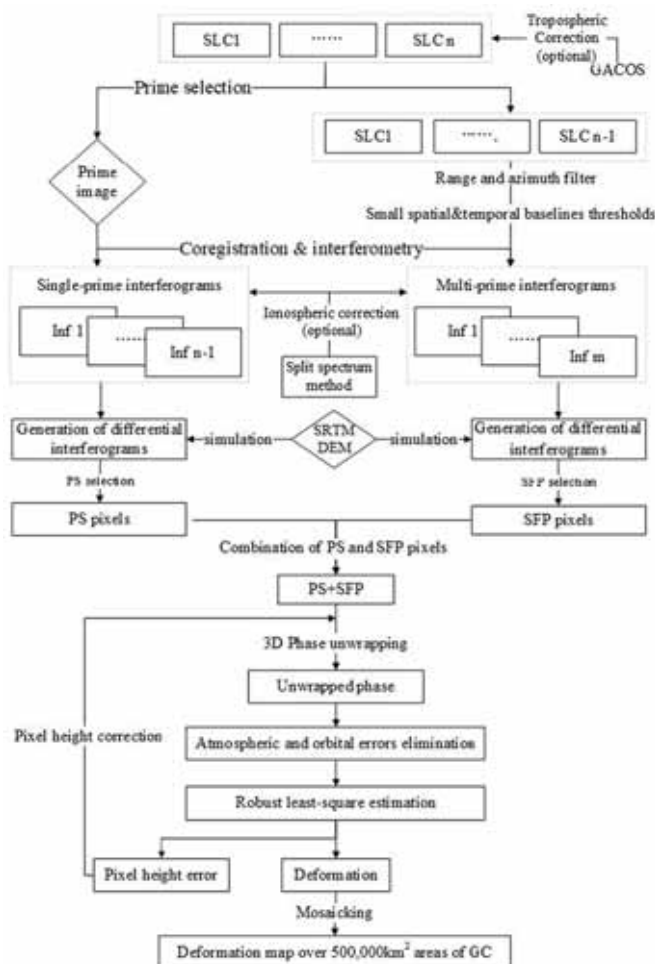
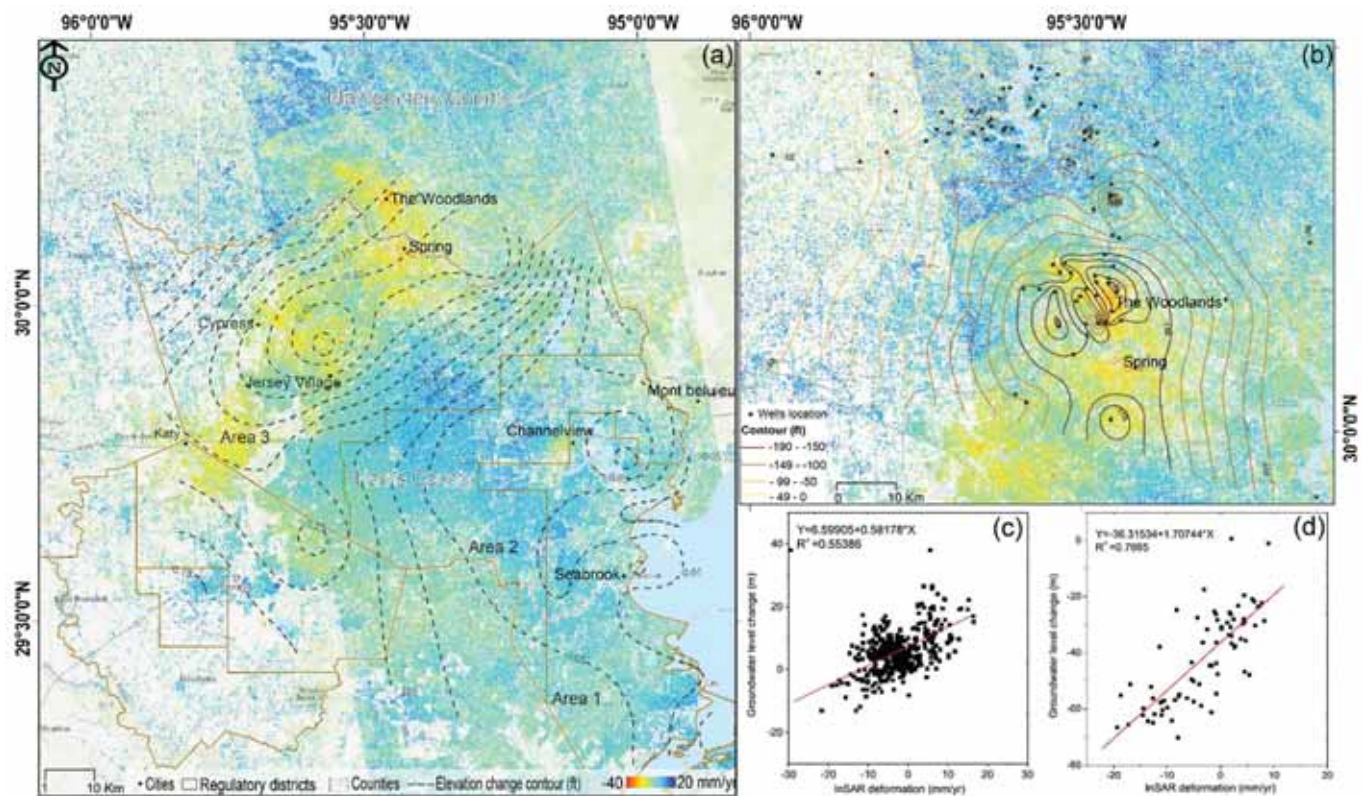


Fig. 2. The deformation mapping processing chain.



**Fig. 3.** Average land surface deformation map of Greater Houston region (2007–2011): (a) InSAR LOS deformation rate. Contours of elevation changes during 2005–2010 derived by GPS measurement (black dashed lines) were superimposed (2). The brown lines display boundaries of groundwater regulatory district of HGSD and FBSD (Fort Bend Subsidence District); (b) Deformation over Montgomery County, where the largest subsidence was observed, along with contours of groundwater level changes at Jasper aquifer for the period of 2000–2011 (3); (c) Correlations between the groundwater level change during 2002–2011 in Evangeline and Chicot aquifers and InSAR deformation; (d) Correlations between the groundwater level change during 2000–2011 in Jasper aquifer and InSAR deformation. The red lines in (c) and (d) are linear regression of these wells. Background: topographic map. (For interpretation of the references to colour in this figure legend, the reader is referred to the web version of this article.)

reached a consensus on spatial and temporal patterns of subsidence with regards to HGSD regulations in Harris, Fort Bend and Galveston Counties (Fig. 3a). Groundwater withdrawal from the Jasper aquifer has been increasing since 2000 as urban growth spreads northward, especially the extensive urban development in Montgomery County, resulting in a groundwater level decline of nearly 60 m in the Jasper aquifer system up until 2015. Over this period, the locus of highest subsidence shifted from northwest Harris County northeastward to The Woodlands and Spring area (Fig. 3). As shown in Fig. 3, there are strong correlations between the ground settlements and ground water depth changes, where the ground surface is typically lowered by the decline of water level. Subsidence near The Woodlands is highly correlated with the spatial pattern of groundwater level declines in the Jasper aquifer. The scatter plots in Fig. 2c and d show correlation between the calculated ground water level change and the occurrence of higher subsidence rates. We used a linear regression to describe the variation of deformation with water level change. The coefficient of determination,  $R^2$ , for the two linear regressions are about 0.55 and 0.77, respectively. Faulting activity was also suggested to be related to the observed subsidence at northwestern Harris County and southern Montgomery County (Qu et al., 2019; Qu et al., 2015). But the strong spatial correlation between groundwater withdrawal and the accelerated subsidence rate, as well as the seasonal variability in GPS data illustrate that the significant large scale subsidence in the Houston area is dominated by compaction of fine-grained aquifer sediments (silts and clays) caused by anthropogenic water use (Bawden et al., 2012; Buckley et al., 2003; Khan et al., 2014; Qu et al., 2019; Qu et al., 2015).

### 3.2.2. Beaumont, TX

Subsidence over the Beaumont region can be traced back to the early 19th century, when large amounts of groundwater withdrawal caused water levels to decline, leading to surface subsidence (generally <15 cm) and saltwater intrusion in regions of concentrated exploitation (Jefferson, 1990). Since the late 1970s, groundwater pumping decreased as the majority of water demands were able to be met through surface water supplies. That shift, in combination with the abandonment of many area water wells that had become contaminated by saline encroachment, allowed groundwater levels to recover and alleviated land subsidence (Jefferson, 1990). Besides, subsidence was also reported at some hydrocarbon production fields, such as Port Acres, Port Arthur, Spindletop, and Port Neches field areas, where groundwater withdrawals were/are not significant, e.g., (Jefferson, 1990; Wang and Loucks, 2002). In 2019, Kruger presented a subsidence map of Southeast Texas using measurements from 340 previously installed NGS benchmarks and recent GNSS during the periods of several decades; this work mapped subsidence, with rates varying between 6 and 15 mm/yr, in several areas of Jefferson County, including Port Neches, Port Arthur, and northwest of Beaumont, TX (Kruger, 2019). Numerous investigations have been conducted in the coastal or wetland areas of southeast Texas, but few researchers keep a watchful eye on the Beaumont area. A maximum rate of subsidence of about 35 mm/yr in the Beaumont metropolitan area, located about 130 km east of Houston, has been observed by our MTI analysis (Fig. 4). At least seven subsidence features, whose locations are marked as numbers with prefix # on Fig. 4, with amplitude larger than 10 mm/yr have been discovered. Particularly, three large-scale circular/elliptical shaped subsidence zones (#15,



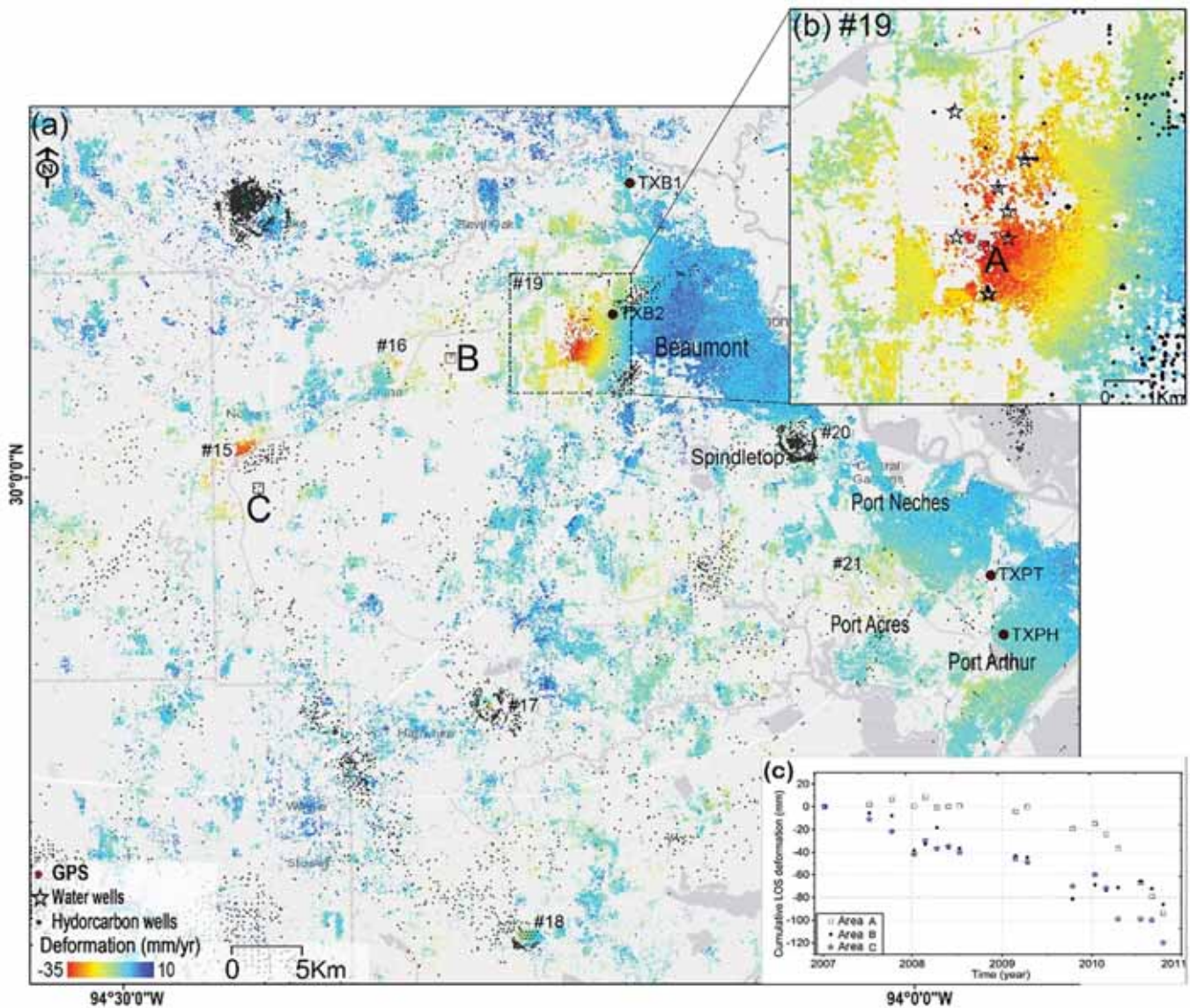


**Fig. 4.** Average land deformation map of Beaumont-Port Arthur (2007–2011): (a) InSAR LOS deformation rate, and hydrocarbon wells (small black dots), GPS benchmarks (dark red circles), subsidence ID (# No.) and cities (names are labeled by black letters) are superimposed; (b) Enlarged deformation map of #19, the hydrocarbon wells (small black dots), water withdraw wells (gray stars) are superimposed; (c) InSAR time-series deformation at areas A, B and C, whose positions are marked as black squares on (a) and (b). Background: Light Gray Canvas basemap. (For interpretation of the references to colour in this figure legend, the reader is referred to the web version of this article.)

#16 and #17 on Fig. 4a), each spanning  $\sim 7$  km in diameter, have been discovered by our InSAR analysis. Both groundwater withdrawal and hydrocarbon production wells (black dots on Fig. 4a) scatter across the discovered subsidence zones (Board, 2020; Texas, 2020), and the subsidence centers nearly follow the distribution of both kinds of wells. Comparing InSAR time-series deformation, water and hydrocarbon well logs provide further insights into the sources that triggered the measured subsidence. Pattern #15 and #16 continuously subsided at variable rates, typically  $>20$  mm/yr (Fig. 4c). A nonlinear subsidence signal was captured by InSAR time-series at Point A and surrounding areas (Fig. 4b, c), where no subsidence was observed during the period of January 2007 and April 2009, but then sharply increased by 100 mm over just one year from late 2009 to late 2010. This elliptical pattern covers about  $13.8$  km<sup>2</sup>, centered near the Beaumont Municipal Airport (Fig. 4b), where more than twenty gas extraction wells and about twenty groundwater withdrawal wells are located. We made careful inquiries into all producing wells and determined that although the hydrocarbon wells did

not begin producing gas until 2014 or beyond (Texas, 2020), water extraction started in 2009. Our time-series observations align with the water production activity at water withdrawal wells (i.e., no active wells in the past, seven wells were drilled in 2009, and  $>10$  wells have been gradually established after 2009). As is illustrated by the gray stars on Fig. 4b, we found that the distribution of water wells that started operation in 2009 corresponds to the spatial spreading pattern of the observed subsidence. In the study area, the Chicot aquifer, which lies in the subsurface at depths of 15 to 150 m and contains a sequence of sand and clay beds, could yield large amount of fresh water (Board, 2020). The wells in 2009 and onward were drilled to the depth of 27–122 m in the Chicot aquifer, where lowering pumping-well water levels led to the compaction of the fine-grained clay layers within this aquifer. Thus, the groundwater extraction should be responsible for the observed local subsidence over cones in area #19.

Our results have quantified contributions from two processes considered influential to subsidence over Beaumont area: withdrawal of

subsurface fluids, including groundwater withdrawal and hydrocarbon extraction. The subsidence over #15 and #16 may have caused by either one of them, or by their combined effect. However, we are confident that the observed subsidence over #19 was wholly induced by production of groundwater for industrial, irrigation, and water use in association with gas productions.

### 3.2.3. New Orleans, LA

There is increasing attention on the potential for ongoing active surface subsidence combined with rising sea levels along the low-lying, unconsolidated New Orleans deltaic plain. Especially since the devastating hurricanes Katrina and Rita, and numerous authors have contributed to the body of knowledge on understanding the subsidence of these areas so as to enhance flood protection measures (Dixon et al., 2006; Dokka, 2011; Dokka et al., 2006; GeoInformatics, 2019; Jones et al., 2014; Jones et al., 2016). However, there are a few papers discussing the use of InSAR techniques to study land stability of New Orleans because of the very challenging coastal environment that decorrelates InSAR signal (Dixon et al., 2006; Jones et al., 2014). Greater New Orleans (GNO) is a Holocene landscape that lies on a combination of distributary channels and lacustrine, swamp, and marsh deposits, comprised of organic matters in variable levels of decomposition. The thickness of Holocene deposits is highly variable throughout the delta, reaching the a maximum of 24 m thick; the much older undifferentiated Pleistocene age deposits lie beneath (Rogers et al., 2006).

Our InSAR-derived four-year-average velocity map (2007–2011) indicates spatial distributions of deformation, such as the subsidence over Lakeshore (south shore of Lake Pontchartrain), Kenner, Algiers, and Harvey communities, all of which are comparable to the rates of subsidence obtained from RADARSAT-1 images during 2002–2005 (Dixon et al., 2006). Our observed subsidence at Michoud, 9th ward, Metairie and along river banks, as well as the slight uplift seen south of

Kenner and West Lake Forest, are identical with the airborne UAVSAR InSAR results from 2009 to 2012 (Jones et al., 2014) (Fig. 5). An average subsidence rate of 5–25 mm/yr occurred over most of the populated areas of GNO. However, no significant motion was observed at Norco through our ALOS result, which was reported as the area of the worst subsidence according to the 2009–2012 UAVSAR results (Jones et al., 2014; Jones et al., 2016). Discrepancies between the two results are likely due to the time differences of two SAR scenes, because high temporal variation in subsidence has been documented at GNO area (Dixon et al., 2006; Dokka, 2011; Jones et al., 2014; Jones et al., 2016). Our work has extended the survey regions to communities located on the south bank of the Mississippi River, and discovered several patterns experiencing higher settling rates than the north bank, including two large patterns at Westwego and Algiers, and several localized cones over Estelle, Harvey and Belle Chasse. The maximum subsidence of ~52 mm/yr occurred at MRGO (Mississippi River Gulf Outlet) canal, where sections of this levee system failed during the storm surge of 2005 Hurricane Katrina. Dixon et al. (2006) reported high rates of subsidence along MRGO levees during 2002–2005 based on RADARSAT images, and raised the possibility of that a high-rate subsidence may promote the levee base breaches. Our ALOS imagery revealed a cumulative subsidence of ~180 mm at section of MRGO levees (white square A, Fig. 5) during the period of 2007–2011, and at least 35 mm/yr subsidence along this levee was also noticed by UAVSAR during 2009 and 2012. Hence, this section of levee system deserves further monitoring to understand its influence on this elongated artificially constructed wall to better assess the potential disaster.

Both the natural and anthropogenic processes, sometimes occurring simultaneously, are cited as initiators of subsidence in GNO, including deep subsidence that could be raised from regional loading of lithospheric faulting, aquifer compaction induced by groundwater withdrawal from shallow upper Pleistocene aquifers, nature sediment

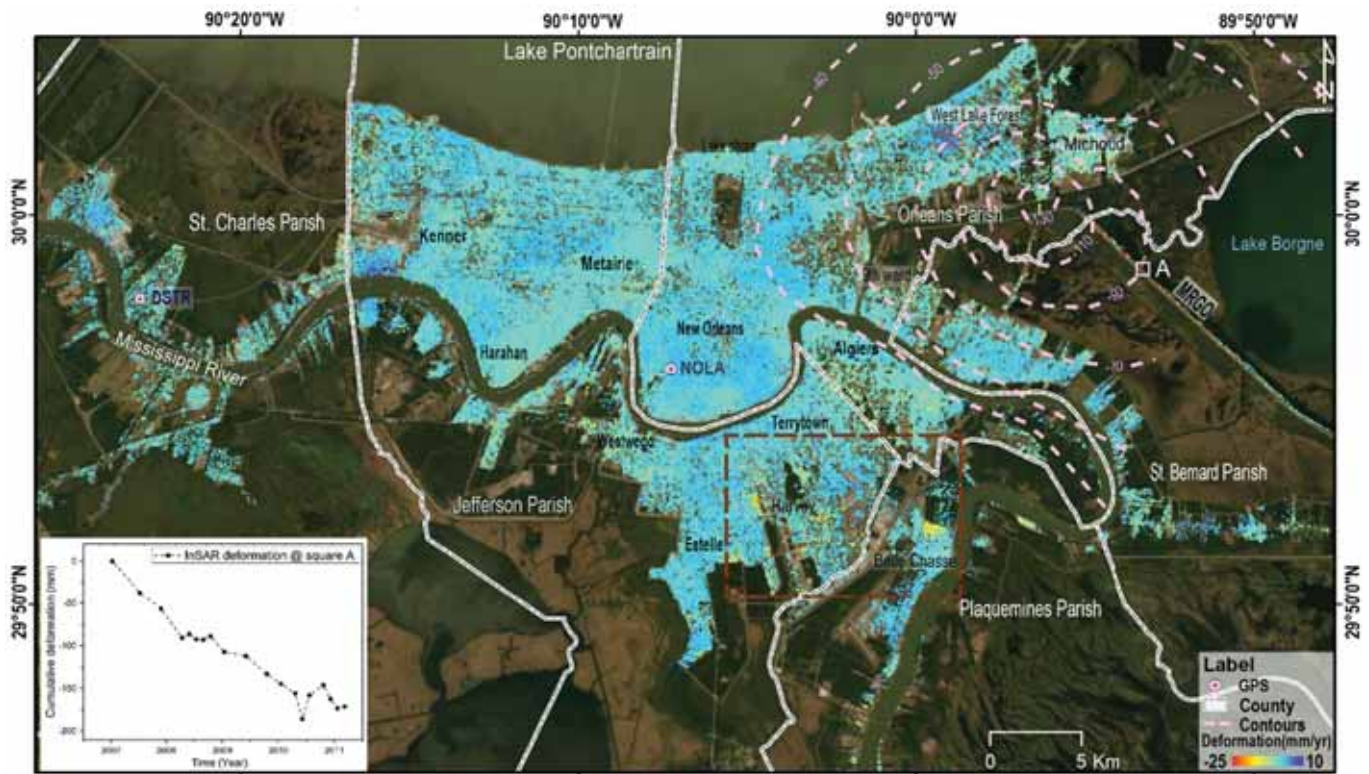
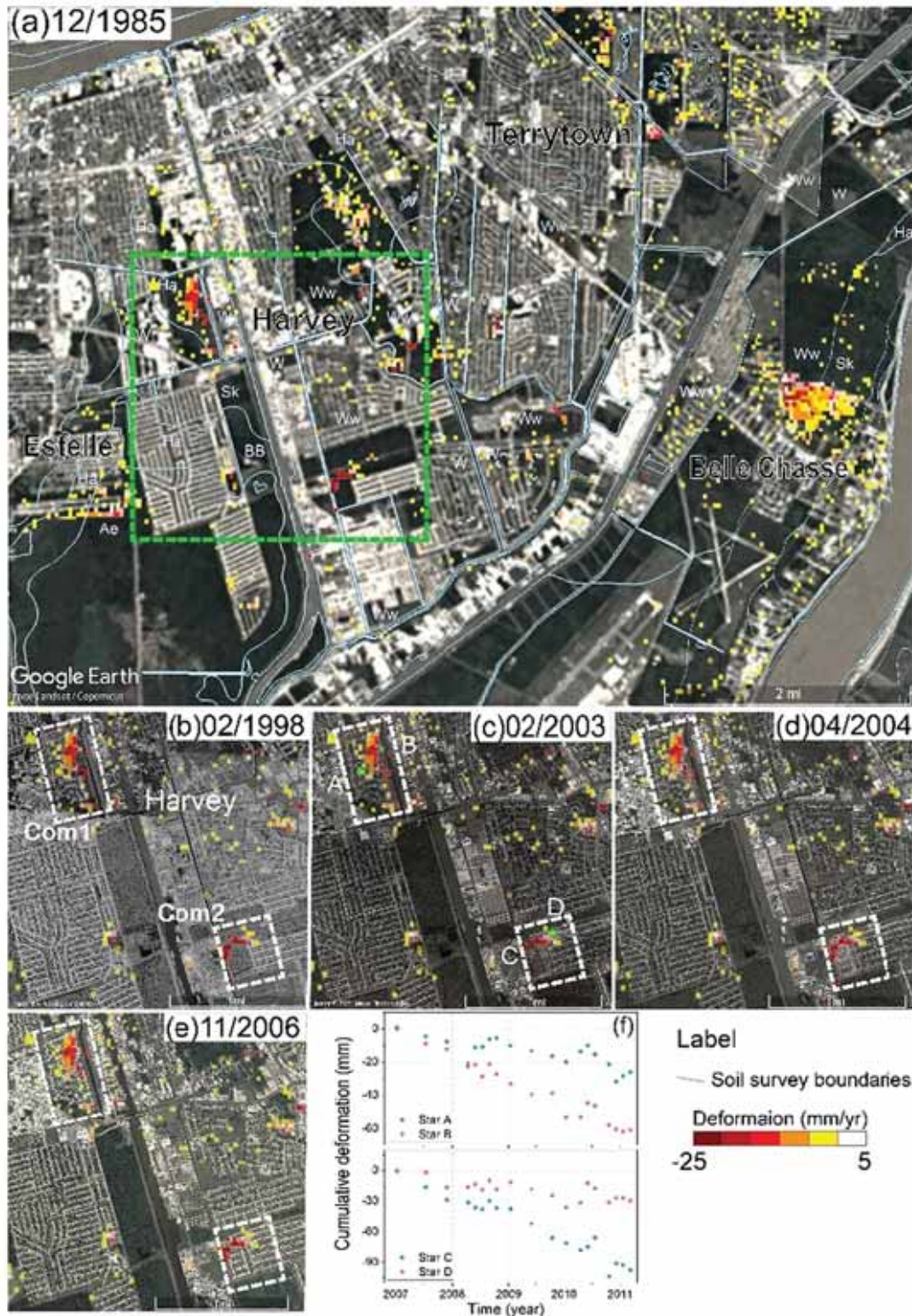


Fig. 5. InSAR LOS deformation rate map of New Orleans region (2007–2011): Parishes (white lines), GPS benchmarks (pink circles), potentiometric contour (pink dashed lines, in feet, digitalized from (LPHI, 2016)), and main cities (names are labeled by black letters) are superimposed; Inset at the lower-left corner shows InSAR time-series deformation at area A (the white square). Background: Google Earth image. (For interpretation of the references to colour in this figure legend, the reader is referred to the web version of this article.)



compaction and surficial dewatering, as well as the drainage and oxidation of organic sediments (Dixon et al., 2006; Dokka, 2011; Jones et al., 2014). Signals of subsidence are recognized around some urban and industrial areas; for instance, in the Michoud area, where factories are clustered, previous work suggested this was associated with massive

groundwater use for production demands (Dokka, 2011; Jones et al., 2014; LPHI, 2016) (Fig. 5). The Michoud region utilized an average of 10.87 Mgal/d for power generation in 2010, and occupied 84% of the entire Orleans Parish's groundwater use. Extraction of large volumes of groundwater from wells drilled to a depth of 192–196 m into the



**Fig. 6.** (a) InSAR-derived subsidence rate of  $>5$  mm/yr is superimposed on optical image of 1985, whose location was marked on Fig. 5; (b–e) Enlarged optical images of 1998, 2003, 2004 and 2006 over two newly-developed communities located at Harvey Parish (Com1 and Com2 on (b)), whose location was marked on (a) as green dashed square; (f) Time-series deformation at green stars A–D, whose location was marked on (c). The light blue lines display the soil survey boundaries from USDA (United States Department of Agriculture), and the small white letters mark the soil types at the ground surface (Agriculture, 2021). Background: Google Earth image. (For interpretation of the references to colour in this figure legend, the reader is referred to the web version of this article.)



Gonzalez-New Orleans Aquifer formed a large potentiometric funnel beneath the industrial plant in Michoud region (Fig. 5) (LPHI, 2016). The subsidence undoubtedly occurred within the vicinity of intensive industrial groundwater extraction during our study period (Dokka, 2011; Jones et al., 2016; LPHI, 2016) (Fig. 5). Lake shore and some other areas on the south shore of Lake Pontchartrain are former marshland with a high percentage of organic matter that were drained and urbanized through canal drainage and land filling. The surface water drainage process could promote soil desiccation (occurs soon after drainage) and oxidation of the drained peat, causing considerable sediment compaction over a period of years (Snowden et al., 1977) (Fig. 5).

The study revealed a high subsidence rate localized to construction-related areas on the south bank of the Mississippi River, mainly Jefferson Parish, providing insight into shallow sediment compaction as a causal factor of subsidence (Figs. 5 and 6). Jefferson Parish, bordered by Lake Pontchartrain to the north and the Gulf of Mexico to the south, has developed large acres of former swamps and marshes for urban use through drainage operations beginning in 1950s. Construction on the reclaimed marshland might have initiated a new round of organic soil consolidation and/or oxidation, especially when the water table was lowered (Snowden et al., 1977). In Fig. 6, pixels with a subsidence rate larger than 5 mm/yr are displayed on optical images from 1985 to 2006 (Fig. 6(a-e)). By comparing the InSAR-derived subsidence with the earliest optical image from 1985, we found subsidence mostly occurred over newly-built blocks on former wetlands (Fig. 6a), and the magnitude of subsidence varied according to the construction activities. Fig. 6(b-e) shows enlarged maps over two newly-developed communities located in Harvey Parish (Com1 and Com2 on Fig. 6b). Construction of Com1 went into operation prior to December 1998 in the southwest part of this community, extending northward no later than February 2003, and construction of the eastern part completed around 2004–2006. Both the west (star A) and east (star B) parts of Com1 show substantial subsidence during the period of 2007–2011, however, the houses built later (star B) show a larger rate of subsidence. A similar situation also occurred at Com2, where larger subsidence was observed over a neighborhood located at the west portion that was built near the end of a development cycle. The subsidence over this area is highly correlated with the construction activities. Time-series results at stars A and C exhibit a nearly constant high rate of subsidence during the period of 2007–2011, i.e., 7–8 years after construction, while subsidence at stars C and D is more moderate and gradually slowed down. In addition, preliminary result from Sentinel-1A/B SAR imagery during 2015–2020 (not shown in this work) continue to show signals of subsidence over these same communities, albeit at a lower rate. This illustrates that the occurrence of shallow sediment compaction over the study area from upward loading could last longer than a decade following the period of active loading (Fig. 6). Our results here suggest that the most likely trigger of the mapped subsidence over GNO are groundwater withdrawal and shallow sedimentary compaction.

### 3.3. Land subsidence introduced by hydrocarbon exploration

Highly active oil and gas production over Texas and coastal Louisiana has led to the ground instability around the hydrocarbon extraction sites. Pressure relief in oil/gas production sites can lead to reservoir compaction, movement of the overburden, and land surface deformation above and/or within the reservoir. >20 subsidence cones with a velocity larger than 10 mm/yr have been detected through our MTI analysis over the GC, and deformation scales vary by location from 1 to 10 kms in diameter. This section will review four particularly striking ground settlement patterns over Hidalgo County, TX, and Corpus Christi, TX, where subsidence had never been observed/reported historically. Average velocity plots for other typical subsidence sites can be found in the Supplementary.

#### 3.3.1. Hidalgo County, TX

Our InSAR results have recognized three subsidence patterns in south Texas' Hidalgo County: the Jeffress Gas Field, the McAllen Ranch Gas Field and an area within the McAllen metropolitan area, each with average velocities larger than 10 mm/yr (#1–3, Fig. 7a). For validation, we compared the time-series deformation from GPS station TXPR for the same period as the ALOS-1 acquisitions with the corresponding InSAR measurement (Fig. 7b). The average velocity indicated by GPS measurements at TXPR is  $-4.9$  mm/yr while the rate for InSAR at the corresponding location is  $-5.2$  mm/yr, suggesting a good agreement between the two deformation observations. The Rio Grande is the principal source of all water uses in southeastern Starr County and Hidalgo County, and a great amount of its supply has gone towards irrigation. Most of the groundwater development in Hidalgo County for irrigation supply is in the central and southern portion of the county, e.g., large amount of irrigation wells located to the southeast of subsidence cone #2, whilst the development for domestic and other uses is scattered sparsely across the county (TWDB 2020; Drillinginfo 2019; Texas, 2020). There is very limited groundwater production over the whole of Hidalgo County, and the water levels in aquifers show no significant decline in depth within a period of years (Ratzlaff, 1980). In fact, the Texas Water Development Board reported a slight increase of nearly 5 m in the groundwater level at State Well No. 87–39-308 from 1933 to present, whose location was marked as a purple dot in Fig. 7a (Fig. 7d). Both InSAR and GPS measurements at TXPR show a consistent time-series of subsidence with little to no seasonal changes. In addition, the spatial distribution pattern of subsidence is not correlated with locations of irrigation wells (Texas Water Development Board, 2020; Drillinginfo, 2022; Texas, 2020). All of the above-mentioned analyses suggest that the observed subsidence cones in Hidalgo County are unlikely to be a consequence of groundwater withdrawal. Petroleum and/or natural gas industry could possibly be the influencing factor for InSAR-measured subsidence at Hidalgo. The areas of subsidence almost exactly conform to the boundary of the productive regimes, and also correlate with the production activities (Fig. 7a). Subsidence at the Jeffress (#1) and McAllen Ranch (#2) gas fields are two of the most widely recognized subsidence features with a velocity of as much as 35 mm/yr during a four-year period in the Lower Rio Grande Valley (Fig. 7a). Both the McAllen Ranch and the Jeffress are the two greatest producing fields with prolific gas production in the study area. The McAllen Ranch Field, situated in northwestern Hidalgo County, has two separate accumulations covering an area of about 31,000 acres. Gas is extracted from the Oligocene-age geopressured Vicksburg sandstones formation at depths of 2836–4697 m in this field. >170 boreholes have been drilled in the reservoir to exploit stratigraphic intervals within the Vicksburg formation from the K to V sands (Cisar and Stovall, 1998). The geopressured reservoirs are estimated to hold the greatest amount of gas, whereas the rock within these formations is weak because of its low effective stress (Stuart, 1970). Beyond that, both the porosity and permeability of this formation is low, as a result, reservoirs are susceptible to compaction and subsequent surface subsidence when extracting large volumes of gas from the producing horizons (Doornhof et al., 2006; Swanson et al., 1976). The sandstone reservoirs of the Jeffress Field are nearly identical with the McAllen Ranch Field, in most aspects. The McAllen Ranch was once a prolific gas field with a production rate of approximately 150 MCF (1000 cubic feet) per day in late the 1960s, but production dropped to only about 24 MCF/D since 1984 (Durrani et al., 1994). Its historically higher production rate may be the reason for the identified large subsidence. Thus, we attribute all the mapped ground subsidence in Hidalgo and Starr Counties to production of gas and associated groundwater withdrawal.

#### 3.3.2. Corpus Christi, TX

Corpus Christi (Nueces County), TX, is a well-known subsidence region with subsidence since 1940s caused by extraction of gas, oil, and associated ground water usage, with >1.6 m of subsidence reported

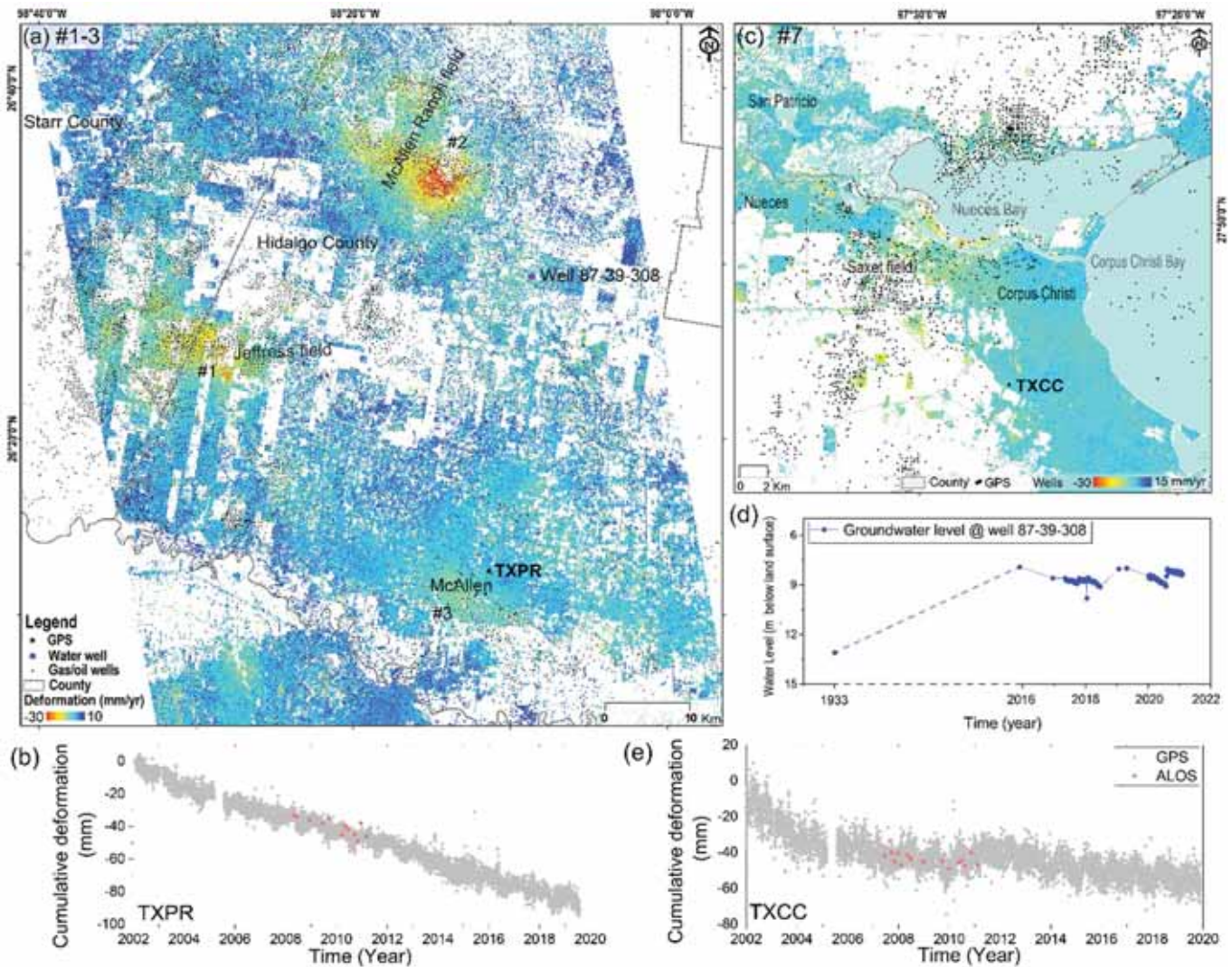


**Fig. 7.** Average land surface deformation map of southern Texas (2007–2011): (a) InSAR LOS deformation rate over Starr and Hidalgo County (Subsidence #1–3); (b) display groundwater level measurement at State Well No. 87–39–308 from 1933 to present; (c) and (d) show time-series deformation measurements at GPS stations TXPR and TXCC respectively; (e) InSAR LOS deformation rate of #7, i.e., Corpus Christi area. Background: topographic map. Hydrocarbon wells (small black dots), GPS benchmarks (black stars), water well (purple circle), cities, counties, and places (names are labeled by black/Gy letters), as well as subsidence IDs (#No.) are superimposed. (For interpretation of the references to colour in this figure legend, the reader is referred to the web version of this article.)

from 1942 to 1975 in western Corpus Christi (Ratzlaff, 1980). Our InSAR analysis has mapped irregularly shaped patterns of subsidence at the south shore of Nueces Bay and western Corpus Christi where the historic land subsidence occurred (Fig. 6c). InSAR measurements report a maximum subsidence of  $\sim 30$  mm/yr at southern Nueces Bay region, where engineered shoreline accounts for much of the bay's land. Subsidence at a rate of about 15 mm/yr from 2007 to 2011 could also be recognized at the Saxet Oil and Gas Field, in Nueces County, TX, 8 km west of Corpus Christi. The areas of subsidence almost exactly conform to the distribution of the productive wells in Saxet Field (black dots on Fig. 7e). Observations from both the tide gauge and the natural beach slopes suggest that natural compaction of the thick sedimentary induced subsidence appears to be relatively trivial as compared to the influence of sediment compaction associated with hydrocarbon production and/or groundwater withdrawal in the Corpus Christi region (Morton et al., 1983). There are a very limited number of groundwater wells around the subsided area, where the water head decline was insufficient to result in a significant altitude loss (Morton et al., 1983; Ratzlaff, 1980). The high spatial correlation between distribution of subsidence and hydrocarbon extraction, and the comparative shallowness of the productive reservoirs

at Saxet Field (1237–2469 m), as well as the absence of groundwater withdrawal illustrate that the oil/gas exploration could be responsible for the observed subsidence at Corpus Christi. As a result, coastal Corpus Christi is notably more vulnerable to sea level rise under the combined action of subsidence and global sea level rise than other coastal areas along the GC.

### 3.4. Localized subsidence due to salt mining

More than one third of the US is underlain by evaporite, leaving large deposits of salt, from which extraction of minerals, either by natural or anthropogenic-prompted processes, can lead to land surface subsidence and may even produce a sinkhole (Ege, 1984). When the evaporite minerals intrude into overlying rocks, Salt domes are formed; in the US, they are principally noticed along the Gulf of Mexico, where over 500 salt domes are scattered in a belt from Texas to Louisiana (Martinez, 1991). The principal salt structure in Louisiana is known familiarly as 'Five Islands', and includes Jefferson Island, Avery Island, Weeks Island, Cote Blanche Island and Belle Isle, all located on the Louisiana GC. The five islands are roughly circular topographic prominences, and are



between 1 and 2 km in diameter, distributed at irregular intervals along a straight line that runs from northwest to southeast (Fig. 8a). Louisiana's five piercement-type salt dome islands, arched up by uplifting solid rock salt that exists underneath the Mississippi river delta, rise up over 23 m above the surrounding Holocene coastal marshes, with Avery Island standing the highest at 46 m above sea level. These islands are the only broad topographic hills among the coastal marshes and swamps of Louisiana, which are abundantly vegetated, and are widely known for salt, gas and oil production (Brian and Lock, 2000; Ege, 1984; Hoentzsch et al., 2019; Neal et al., 1993). The Five Islands has been actively mined for salt since the 1900s using the conventional room and pillar system. For instance, the Cote Blanche salt mine is one of the three leading salt mine producers in Louisiana, and yields about 15% of the de-icing salt for US's highways (Brian E. Lock 2000). As with all other underground production activities, the extraction of rock salt from subsurface mines is highly risky, and hazards frequently occurred in room and pillar mining work because the system is routinely operated with heavy equipment. Despite this, almost all salt mining at GC operates on the room and pillar strategy. The room and pillar system has several levels at discrete depths, and consists of a grid of corridors spaced by pillars of salt, covering few square kilometers, at each level (Brian E. Lock 2000; Hoentzsch et al., 2019; Neal et al., 1993).

Average deformation rate maps from two InSAR paths recognize subsidence of  $\sim 60$  mm/yr at three of the five islands, i.e., Avery Island, Weeks Island, and Cote Blanche Island, while no detectable deformation

is evident at Jefferson Island and Belle Isle (Fig. 8b). Even though no instrumented subsidence measurement was reported from the Five Islands previously, evidence of subsidence includes sinkhole ponds of several hectares, ten-hectare-size topographic saddles, and kilometer-extent collapse structures at Avery and Weeks islands (Autin, 2002; Brian E. Lock 2000; Hoentzsch et al., 2019). Because the southern four islands are either entirely surrounded by marsh land or are partially sea marshes alternating with water embayments from the Gulf of Mexico, combined with the presence of a few large ponds, the density of InSAR pixels is limited in study area. Jefferson Island, rising from dry plains, faces Lake Peigneur to the north and overlies the vast majority of surficial Jefferson Island salt dome. In addition, Belle Isle salt dome is identical with Jefferson Island in residing mostly beneath lakes. As a result, only a small number of coherent InSAR pixels was detected along edges of these two islands, and hence they are insufficient to detect any potential signal that reflects several operations beneath salt dome structures. A maximum rate of subsidence of 30–60 mm/yr occurred at the center of the mine on all three islands, paralleling nicely to the location of the salt mining works (Figs.8(c-f)). Subsidence occurred within the vicinity of the mining scope (black lines on Figs.8(c-d)) at Avery and Weeks islands, decreasing towards the margins of the salt extraction areas (Figs.8(c-d)). Subsidence over an area of approximately 1.5 km by 1 km is observed at west central Cote Blanche Island by two neighboring tracks of ALOS data with generally good agreements on spatial spreading and magnitude of subsidence (Figs.8(e-f)). However,

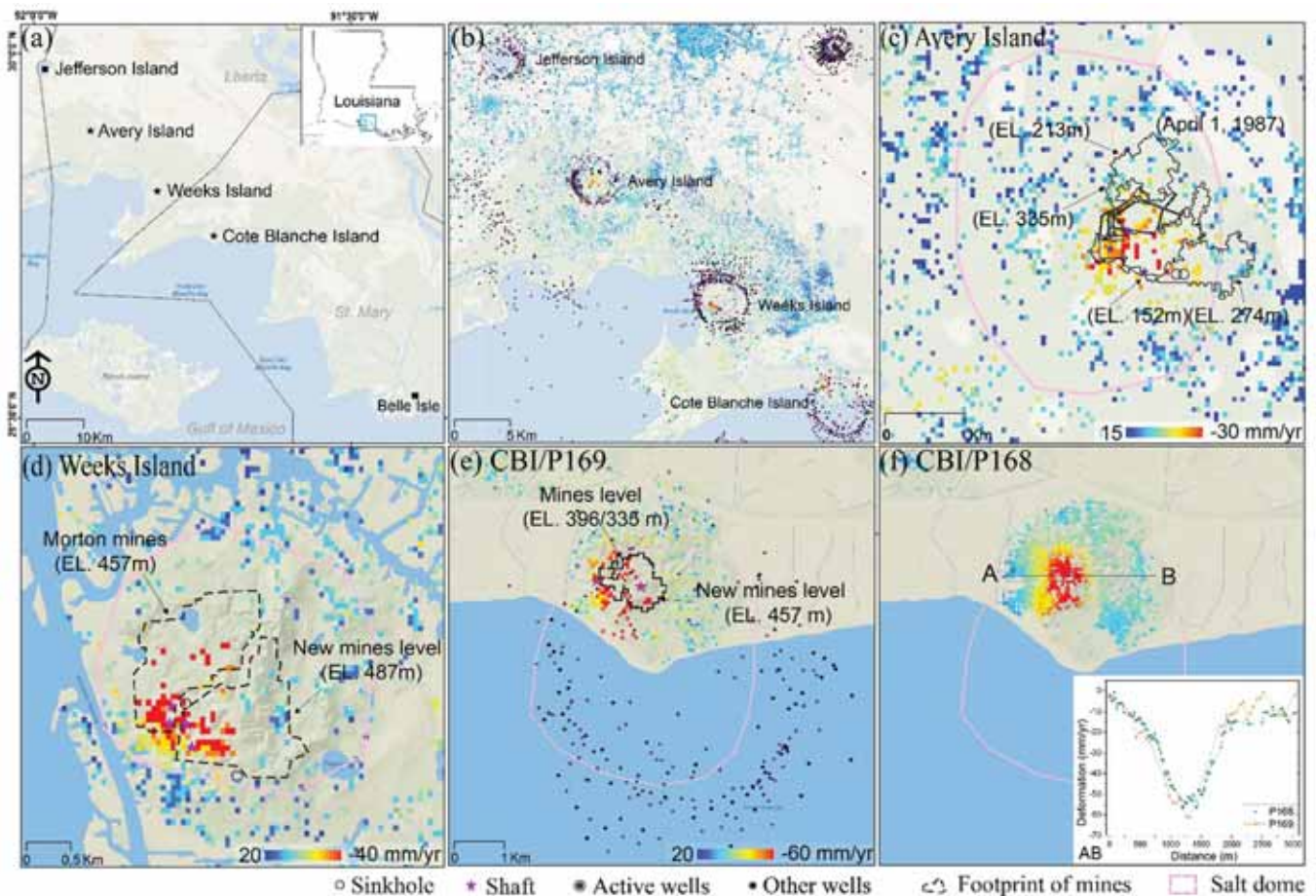


**Fig. 8.** Enlarged average deformation maps (2007–2011) at the Five Islands. (a) shows the geographic position of the Five Islands, while (b) displays InSAR average deformation rate at the four north islands; (c–f) illustrate deformation maps at Avery Island, Weeks Island and Cote Blanche Island (CBI) separately. Background: topographic map. Hydrocarbon wells (small black dot), sinkholes (black circle), shafts (purple star), cities, footprint of salt mine (black dashed polygons), and places (names are labeled by black/Gy) are superimposed. InSAR deformation across Cote Blanche Island salt dome is an inset on the down-right, whose position is marked on (f). (For interpretation of the references to colour in this figure legend, the reader is referred to the web version of this article.)

subsidence occurred beyond the confines of the mine extent at Cote Blanche Island. We should note that the extent of the salt mine activity (black lines on Fig. 8) are modified from previous literature published in 1976, 1987 and 2019 separately (Brian E. Lock 2000; Hoentzsch et al., 2019), and the outer margins of the salt domes (pink lines on Fig. 8), as obtained from USGS's 2004 publication (Huffman et al., 2004), all of which are not geometrically accurate images of the scopes of current operational levels. Thus, some discrepancy of spatial distribution between the measured subsidence and salt mine footprints is likely due to either the antiquated profiles of mining operation and/or the complicated framework of the salt rocks themselves. InSAR identified subsidence of  $\sim 40$  mm/yr at western Weeks Island, corresponding to the site of active salt mining using a conventional room and pillar mining method, in stark contrast to no visible subsidence observed in the eastern part of the island where the salt has instead been extracted using a solution mining method for the past several decades (Hoentzsch et al., 2019). Subsidence is more frequently encountered in room and pillar mining works due to the heavy-duty equipment commonly applied in this system. A number of oil/gas wells, located at the outer margins of the Five Island, withdraw oil/gas from reservoirs at flanks of the salt dome (60), but no obvious subsidence can be found through InSAR imagery near these wells. The high spatial correlation between distribution of subsidence and the conventional salt mining systems, the

comparative shallowness of the mining works at all five islands (i.e.,  $\sim 500$  m), as well as the absence of oil/gas exploration within the immediate vicinity of subsidence demonstrates that the conventional salt mining room and pillar method relying on heavy machinery in the subsurface could be responsible for the observed subsidence at Avery Island, Weeks Island, and Cote Blanche Island.

### 3.5. Surface uplift due to injection/disposal and gas storage

#### 3.5.1. Injection/disposal induced uplift

Just as extracting underground fluids may lead to land subsidence, injecting fluid into subsurface reservoirs often leads to surface uplift (McGarr et al., 2015; Shirzaei et al., 2019). Injection-induced pore pressure change within the scope of injection leads to a depression of effective stress on the skeleton structures and thus expansion of the geologic formations (McGarr et al., 2015). These uplifts are usually localized, small in size (0.5–2 km wide), and rapidly developing (cm/yr) (Fig. 9a), but are usually inconspicuous for a long period, primarily because disposal wells are generally located in uninhabited areas. However, the increasing rate of seismicity over the past two decades in areas of the eastern/central US with little or no previous documented history of detected earthquakes, has aroused public concern over nearby human activities, such as fluid injection, that may play a role in this

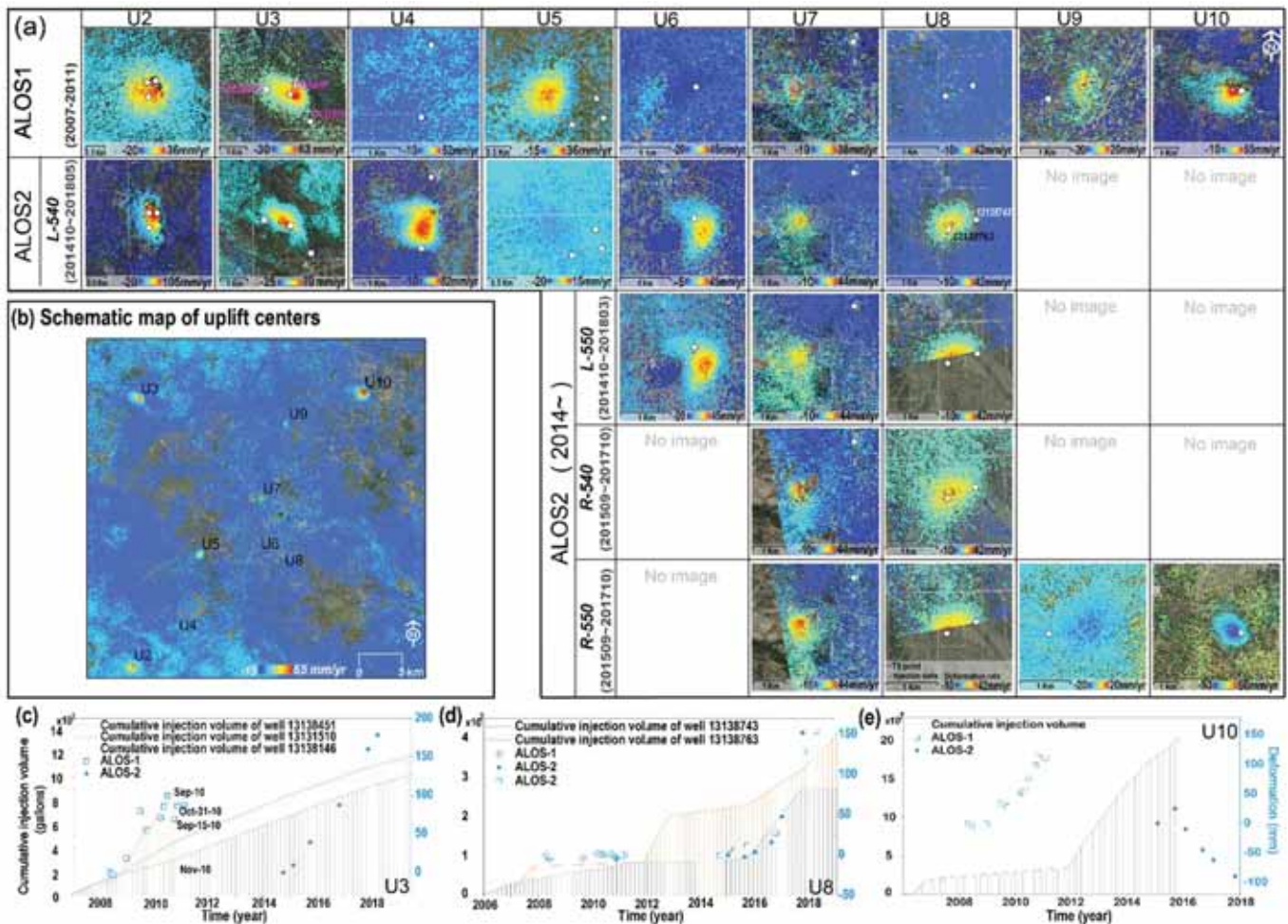


Fig. 9. (a) Enlarged average deformation maps around injection wells (white dots). The rows are sorted by 5 SAR datasets (1 ALOS frame and 4 neighboring ALOS2 frames), while the columns are sorted by subsidence ID (#Nos.). 'No image' denotes this site is not covered by SAR image. Background: Google Earth image. Different colour scales are used to highlight the deformation in subfigures, and the cold-colored (from dark blue to light) pixels show LOS subsidence to small LOS uplift, while the hot colors (yellow to red) show large LOS uplift (i.e., deformation towards the satellite). (b) Schematic map of uplift patterns, whose location is marked as dashed rectangle on Fig. 1. (c-e) Time-series cumulative deformation at U3, U8 and U10, as well as the volume of injected wastewater (gray and pink bars) of the corresponding wells are list at the bottom. (For interpretation of the references to colour in this figure legend, the reader is referred to the web version of this article.)



phenomenon (Kim and Lu, 2018; McGarr et al., 2015).

We processed SAR images from one ALOS-1 (2007–2011) (hereinafter Phase-1) and four different ALOS-2 (2014–2018) (hereinafter Phase-2) frames separately, generating five line-of-sight (LOS) deformation rate maps, and identified significant uplift signals with amplitudes ranging from 3 to 10 cm/yr mainly over Duval County of South TX. At least 11 cones of uplift that are roughly circular in shape and typically span ~2 km in diameter have been discovered, almost all of which had never been noticed and reported before this study (Fig. 9a). We sorted out some results in the sheet embedded in Fig. 9, displaying the deformation locations (labeled as ID# on Fig. 1) as the rows and the data source as the columns. The observed features vary in magnitude, spatial extension (round, ellipse, or crescent-shaped) and temporal evolution from injection to injection, but coincident measurements were reported from 4 independent ALOS-2 frames; these appear in the deformation maps listed at the 5th, 6th and 7th columns in Fig. 9a. Minor discrepancies in amplitude of deformation at #U6, #U7 and #U8 could be attributed to the different time-span of SAR acquisitions and nonlinearity of the deformation. Regarding temporal variation, InSAR recognizes an overall pattern of uplift during Phase-1, and a structural feature of subsidence since 2014 at sites #U5, #U9 and #U10. Uplift signals occurred only in Phase-2 at sites #U4, #U6 and #U8, while a constant rise of ground surface was observed during the whole study period at sites #U2, #U3 and #U7. However, regardless of the evolution of the feature, all of the observed uplifts are centered at or <2 km away from injection well location(s), as marked with white circles, and agree well with the production activities of these wells (Fig. 9). The high temporal and proximal association indicate that the surface uplifts are related to underground fluid injection activities of nearby wells. To analyze the derived patterns, we plotted surface movements and injection volumes versus time for three representative deformation sites, i.e., #U3, #U8 and #U10, to highlight different trends in their own development (Fig. 9c-e).

Our InSAR results reveal an asymmetric elliptical surface uplift at site #U3, covering a region of about 2 km by 1.5 km elongated towards the southeast, where there are three closely spaced injection wells (Fig. 9a). These wells are classified as Class II injection wells for disposal of saltwater into the subsurface as a result of oil/gas production (API No.13131510) and for injecting brine or other fluids into oil-bearing formations to enhance recovery of hydrocarbons (API Nos.13138451, 13,138,146) (Texas, 2020). About 120, 100, and 80 million gallons of saltwater were injected into reservoirs at depths of approximately 305, 213, and 700 m through wells 13,138,451, 13,138,146 and 13,131,510 respectively. The uplift rate remained relatively stable at about 60 mm/yr until Aug, 2010, reflecting that the surface rises along with active injection operations of the nearby wells. However, when injection ceased at well 13,131,510 in Sep, 2010, the cumulative deformation sharply decreased by ~20 mm, i.e., a very short-term subsidence occurred, that is followed by another gradual uplift during the rest of Phase-1 and Phase-2. The extent of uplift was slightly shrinking and migrating towards the northwest during Phase-2, and the maximum uplift center transferred from east to the northwest of well 13,138,146 (Fig. 9c). All these characteristics suggest that the observed uplift signal is connected with activity of well 13,131,510, however it was not the sole factor because the surface elevated at comparable rates prior to and following the injection halt. Contributions from all three nearby wells are considered influential to the uplift over site #U3, but the specific contributions of each well are yet to be ascertained.

Measurements from 4 individual ALOS-2 frames confirm the uplift at #U8 during Phase-2. The ground elevated gradually at first, but then as accelerated in response to the sharp increase in injection volume at both wells 13,138,763 and 13,138,743 around late 2015 (Fig. 9c). A comparison between the observed uplifts and injection records of these two wells illustrates that the uplift tendency displays clear linkages to the injection activities, i.e., the higher volume of the injection, the higher uplift rate is. However, #U8 continued gradual uplifting, reaching about

150 mm by early 2019 even after well 13,138,763 ceased operating a few months before in Oct, 2018, suggesting that the measured deformation is most likely triggered by well 13,138,743. We use a linear regression to describe the uplift with the injection volume at well 13,138,743. The coefficient of determination,  $R^2$ , for the linear regression is about 0.88.

Surface uplift of ~65 mm/yr was observed at #U10 during Phase-1, where one injection well (13100791) was located in its vicinity. This well is classified as Class II injection well for disposal of saltwater into the underground at depth of about 610 m as a result of oil production. The coefficient of determination,  $R^2$ , for the linear regression, that describes the uplift with the injection volume at well 13,100,791 during Phase-1, is about 0.89. But no data was reported for this well since Dec, 2015, whose status was flagged as 'DELINQUENT' ever since. This area experienced a slight uplift during 2015, and then showed continuous subsidence reaching about 100 mm at the end of the SAR observations with a declining rate (Fig. 9d). The appearance of subsidence corresponds to the beginning of the 'blank period' of this well, suggesting injection at well 13,100,791 was very likely shut down since Dec, 2015. Pore pressure within the subsurface disposal formation will drop after shutdown of injection activity owing to fast pressure dissipation, resulting in gradual compaction of the dilated reservoirs and thus ground subsidence (Bohlooli et al., 2018; McGarr et al., 2015; Shirzaei et al., 2019).

### 3.5.2. Gas storage caused uplift

Underground storage facilities play a significant role in managing the delivery and supply chain of fossil gas. Most underground gas storage facilities are located in depleted reservoirs in oil/gas fields, aquifers, and salt cavern deposits. Salt caverns that are leached or mined out of underground salt formations are perfect containers for underground gas storage because of their capabilities of high deliverability and quick replenishment, with 4% of the working gas capacity in the US in such facilities. Most salt cavern storage facilities have been developed in salt dome formations located along the GC; the North Dayton salt dome gas storage facility in Liberty County, TX, operating since 1986, is one of them. During the circulated operations of injection/withdrawal into/from a salt cavern, the cavern's temperature change, together with the change in operating pressure, could change the effective stress on the cavern wall, leading to ground surface displacement (Fig. 10). Our InSAR observations indicate the deformation over the North Dayton salt dome is complex: a localized uplift feature occurs over the storage facilities, and is surrounded by a regional subsidence (Fig. 10). Despite deformation of the cavern fluctuations over time, time-series deformation at #U13 indicates a very slight uplift of about 20 mm during the period of 2007–2011 (gray squares on Fig. 10e). When analyzing the time-series deformation in the uplift area at the site of the wellbore (black star) in relation to the surrounding regional subsidence (green star), we discovered #U13 had risen by approximately 90 mm during 4 years. The observed uplift fluctuates over time, responding to the seasonal nature of gas injection operations in summer (Fig. 10e). We attribute the recognized localized uplift signal over the North Dayton salt dome gas storage facility to the circulated operations of injection/withdrawal into/from the salt cavern.

## 4. Discussion

### 4.1. The realized uplift signals over South Texas

Injection into or production from the nearby reservoirs may affect reservoir pressure and thus cause surface movement around the injection/production wells. At least 11 uplift features have been identified over South Texas through our InSAR analysis. These discovered patterns are distributed over the Jackson-Yegua Barrier/Strandplain sandstone play of the southern Texas Gulf Coastal Plain, which is basal Oligocene in age and characterized by well sorted, laterally continuous layer of

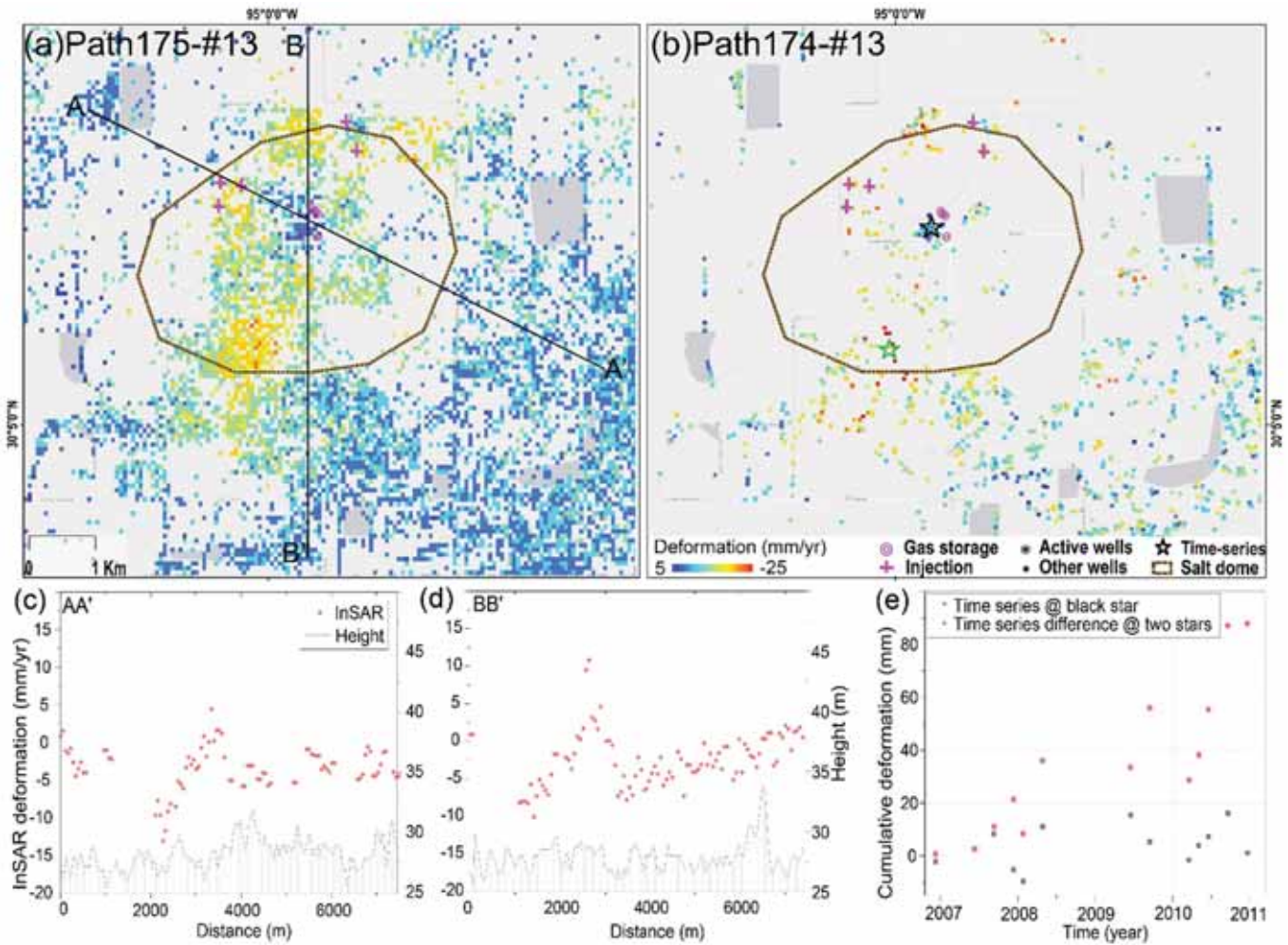


**Fig. 10.** (a–b) enlarged average deformation maps (2007–2011) at North Dayton salt dome whose locations are marked as #13 on Fig. 2 from neighboring ALOS tracks 175 (a) and 174 (b). Background: Light Gray Canvas basemap. Light purple ellipsoids display the position of salt domes. Pink circles represent storage wells, while the dense black dots show distribution of hydrocarbon exploration wells. Detailed description of wells can be found in Drilling Info's database and Texas RRC. (c) and (d) show deformation and topographic height along profiles AA' and BB'. (e) time-series deformation (gray squares) at #U13 (black star on (b)) and time-series deformation difference (red dots) between the areas that marked by black and green stars on (b).

sandstones. The Jackson-Yegua play has a high liquid yield trend and has been the site of active exploration of oil/gas reserves over several decades. However, it is typified by low-level recovery efficiencies with a recovery factor of about 38% playwide (Hamilton, 1995). Secondary recovery techniques are conventionally employed to facilitate the weak solution drive by injecting gas and/or water into known reservoirs at relatively shallow depth to maintain reservoir pressure (Hamilton, 1995).

Significant spatial and temporal correlation between the measured displacement and injection activities implies that the discovered uplifts were induced by saltwater injection through the wells (Fig. 9). Greater cumulative surface displacement mostly occurs at the well(s) with larger injection volume and/or rate (Fig. 9). Rare exceptions on the total deformation are likely attributable to the heterogeneous coefficient of thermal expansion and compressibility of reservoir rocks (Shirzaei et al., 2016). The detected uplift features are complicated, and some of them present asymmetric patterns, such as #U2, #U3, #U4, #U6 and #U8, where more than one injection/productive well is active at a site. The centers of uplift are generally offset from the injection point(s), nevertheless, the magnitude and direction of offsets vary case by case. The injection wellbores are generally established in positions that could best force petroleum towards the production wells from one or several sites around the exploited well to maintain/increase the reservoir pressure.

Injected fluid moves across the underground formation, and pushes oil towards the producing wells. The location and shape of the measured surface uplift patterns might reflect the orientation and extent of the injected liquid flow, and their offsets from the wellbores suggest that the injected fluid may distribute asymmetrically with regard to the injection point(s) (Haase and Stow, 1988). Noticeable uplift/subsidence was observed up to 2 km away from the wellheads (e.g., #U7), which may also demonstrate the far extent to which fluid pressure perturbations can propagate (Ellsworth, 2013). Fluid pore pressure within the connected hydrologic layers might increase as the wastewater was injected into the formations for disposal use, and the perturbation in pressure could diffuse miles away over time (Shirzaei et al., 2019). Definitely, we do not exclude the possibility that other unregistered injection well(s) or hydraulic-fracturing production existed within the vicinity of uplifts and/or the misdeclaration of locations of wellbores.

The observed uplift patterns mainly are located in a Barrier/Strandplain sandstone reservoir of the Jackson-Yegua trend located in northwestern Duval County, which lies along the underlying Wilcox fault zones in South Texas. Various subtle structures and small faults within the overlying Jackson Group, developed with regards to the reactivations of older growth fault lying within the lower Wilcox Group (deeper than 2500 m), have disrupted heavy-oil deposits continuity, which played critical roles in supplying secondary structural traps in the



Jackson Group (Ewing et al., 1986). It should be noted that most of the groundwater wells in the Jackson-Yegua barrier are 91 m or less in depth. The majority of the oil production depths range from 400 to 2000 m beneath the ground surface, since both the ash yield and sulfur content in Yegua-Jackson trend sandstones are generally higher than those of the underlying Wilcox trend. The target injection depths stretch from 213 m to 773 m below the surface for the majority of wellbores in our study area, except for the two situated neighborhoods of #U5 (west well, 1158 m) and #U7 (1767 m) (Baker, 1995; TWDB 2020; Drillinginfo 2019; Ewing et al., 1986; Texas, 2020). A large amount of subsurface fluid injection can increase pore fluid pressure in the connected hydrologic systems and create stress within the reservoirs as well as the surrounding rocks. The reduced effective stress along faults can then prompt the faults to approach a fracture stage and perhaps even trigger earthquake occurrence. The study area experienced long-term surface uplift due to fluid injection but no perceptible seismicity was reported within the vicinity of reservoir bodies. There are various explanations for the absence of seismicity. First, a lack of favorably-oriented, critically-stressed fractures/faults at the immediate vicinity of injection wellhead(s), that ought to be hydraulically communicated with the injection wellbores, is one potential interpretation for the absence of seismic events. Second, according to previous research on induced seismicity, most induced earthquakes happen in underlying basement rocks (Shirzaei et al., 2019). However, the injection facilities in this study area are in shallow deposits, i.e., upper Jackson Group; pore pressure changes in shallow formations without critical faults are less likely to trigger massive seismicity, especially in regions with few to no history of documented earthquakes (Van der Baan and Calixto, 2017). Third, the injection volume into the formation, including saltwater disposal and/or hydraulic fracturing volumes, is another important factor in determining if a place is susceptible to earthquake hazards. In general, the higher the volumes of injected fluid, the greater the risk of induced seismicity in a given area (Van der Baan and Calixto, 2017). And while the volumes at these sites do appear large and/or rapid enough to have deformed the surface, the total injected volumes are lower in comparison to some reported cases where significant induced seismicity occurred, e.g., (Shirzaei et al., 2019; Van der Baan and Calixto, 2017).

#### 4.2. Factors influencing surface subsidence in GC

InSAR can provide unparalleled high-resolution and continuous spatial coverage of the subsidence in GC. According to both the InSAR and GPS measurements, a surface subsidence rate larger than 10 mm/yr occurred at several metropolitan areas, oil/gas exploration fields and salt domes in GC, with the maximum rate of subsidence reaching 56 mm/yr at the Stratton Ridge Oil Field, TX. The discovered zones of subsidence are distributed discretely in the Rio Grande embayment (Oligocene), the Houston embayment (Paleocene-Eocene), and the Mississippi River embayment (Miocene to present) (Fig. 1) along the GC (Swanson et al., 2007). The water-bearing layers of the aquifer system beneath are composed primarily of horizontally and vertically discontinuous fine-grained to coarse-grained sands and gravels with complex interbedded silts and clays (Ashworth, 1995). Layers of fine-grained clays and silts contain an abundance of groundwater storage capacity and confine the coastal aquifers on account of their high compressibility and porosity. The sediment of these regions is fundamentally unconsolidated or semi-consolidated, which is typified by excess pore water pressure at depth, and has been experiencing fairly continual consolidation (Ashworth, 1995; Baker, 1995; Chowdhury and Turco, 2006). It is acknowledged that natural processes, such as sediment compaction, sedimentary loading, faulting, as well as salt mining, contributed to land subsidence of the GC basin (Dokka et al., 2006). Different types of natural processes are not completely independent from one another, and these processes may in fact interact with one another. During the last few decades, the average rate of natural subsidence along the Texas and

Louisiana coasts, principally induced by consolidation of the natural unconsolidated/semi-consolidated formations, is 0–6.5 mm/yr. The Texas coastline is subsiding at an average rate of 1.4 mm/yr, with the most rapid subsidence of up to 6.5 mm/yr at the Mississippi River delta (Dokka et al., 2006; Zhou et al., 2021). The significant subsidence observed at the Mississippi River delta is promoted by the large volumes of fluvial sediment introduced by the Mississippi River during modern delta plain construction (Dokka et al., 2006). In contrast, InSAR-observed rates of subsidence associated with anthropogenic sources, which can be up to 56 mm/yr, are several orders of magnitude higher than the reported natural subsidence processes (Fig. 1). The characteristics of smaller amplitude and longer spatial-wavelength of the natural sediment compaction over GC make it difficult to image from InSAR (Lu and Dzurisin, 2014). The very small deformation (few mm/yr), which could be regarded as background rates on Fig. 1, is below detectability of our InSAR dataset in most instances.

Compaction is a natural process common to nearly all types of sediment once deposited. The young and compressible deposits in GC are essential for subsidence to develop, but other factors also control the occurrence and distribution of the detected significant subsidence. Alterations in land and water use, such as construction, underground fluid (groundwater/oil/gas) extraction and salt mining, following from population growth, urbanization and industrial development through the sedimentary coast, can change the belowground hydrological system and/or increase earth surface loading, sequentially magnifying natural subsidence or initiate new anthropogenic subsidence (Galloway et al., 2008; Galloway and Burbey, 2011). The long history of large-scale human activities, coupled with the unique nature of GC sediments/aquifers, has produced a perfect storm for land subsidence, e.g. (Galloway et al., 1999; Jones et al., 2016; Qu et al., 2019; Qu et al., 2015). The majority of the water usage in GC comes from underground aquifer systems, with >1.3 billion m<sup>3</sup> of groundwater withdrawn from these aquifers every year (Chowdhury and Turco, 2006). Over-exploitation might cause broad groundwater level declines, and induce underground fine-grained sediment (silts and clays) consolidation, consequently triggering aquifer compaction (Galloway et al., 1999). Some detected subsidence features occur in/near densely urbanized areas with high groundwater demand for domestic, industrial, and/or hydrocarbon production use is responsible for subsidence in Houston, New Orleans, and Beaumont (Galloway et al., 1999; Jones et al., 2016; Qu et al., 2015). The highest rates are usually observed over regions with more anthropogenic impacts, and subsidence rates decelerate or return to the very slow background rates when human-induced activities slow or stop. Conversion from groundwater pumping to surface water usage, coupled with the subsidence-management program, has slowed or stopped the severe subsidence near the coastal areas between Houston and Galveston County, as well as the Pasadena-Houston Ship Channel area since 1975. Subsidence continued at high rates in the rapidly expanding northern part of Houston, where high rates of groundwater withdrawal continued during 2007–2011 (Fig. 3) (HGSD, 2013a; Qu et al., 2015; Wang et al., 2017). In the Beaumont region, groundwater pumping has decreased since the late 1970's after surface water became the primary source to satisfy demand. Many wells in this area have been abandoned due to saline water encroachment, leading to recovery of groundwater levels and alleviation of land subsidence (Jefferson, 1990). However, the newly-discovered subsidence over #19 was wholly induced by production of groundwater for industrial/domestic use, and the rapid increase in rate corresponds closely to the water extraction activity since 2009. No obvious subsidence was observed at some of the reported historical subsidence zones induced by groundwater withdrawal, such as Orange County, northern Sabine Pass, northwestern Jefferson County, southeastern Jackson County, northwestern Matagorda County, Lake Charles and Baton Rouge, during 2007–2011, e.g. (Dokka et al., 2006; Galloway et al., 1999; Geo-Informatics, 2019; Konikow, 2015; Morton, 2003; Morton et al., 2006; Paine, 1993; Ratzlaff, 1980; Seifert and Drabek, 2006; Zhou et al.,

2021). It could be that subsidence over these regions appeared at a rate below our recognition threshold of 10 mm/yr or absolutely ceased. The absence of significant subsidence may be a consequence of a lower depletion rate of groundwater. However, high rates of subsidence still occur in many regions where relatively low amounts of groundwater were pumped but with active oil/gas production facilities, and the observed rate in these areas is significantly larger than the estimated natural subsidence. Oil and gas reservoirs over GC have relatively small permeabilities and porosity, and the reduction in fluid pressure in the producing zones may be 20 times greater than that of groundwater reservoirs. Land subsidence above/within these reservoirs are typically large-magnitude, small-sized, and rapid development (Kim and Lu, 2018). Subsidence due to gas/oil extraction is observed over >20 production fields located in Hidalgo County, Corpus Christi, Stratton Ridge, Sarita, Mont Belvieu, Refugio, Victoria, Port Arthur and some oil/gas fields in southern Louisiana (Figs. 1 and 7).

We have recognized at least 30 locations along the GC experiencing notable subsidence during 2007–2011, that are mainly distributed in the Rio Grande embayment, the Houston embayment, and the Mississippi River embayment (Fig. 1). It is possible or even probable that we missed additional regions where InSAR pixels are sparse or not available due to phase decorrelation, as well as regions subsiding at rate below 10 mm/yr. Lacking of significant subsidence in the remaining major urban areas could principally be accounted for by the absence of compressible deposits (Chaussard et al., 2013). In part of middle coastal Texas, middle Louisiana, southern Mississippi and Alabama, as well as western Florida, surficial features are dominated by (fine) sandy loam, loamy sandy or silt, which are relatively incompressible or less compressible compared to the clay deposits (Agriculture, 2021; Ashworth, 1995; Baker, 1995; Huffman et al., 2004). Significant subsidence is therefore unlikely to develop over cities seated on these types of sediments, which is in accordance with the absence of subsidence in Tallahassee, Dothan, Hattiesburg, Alexandria, and even some coastal cities, such as Panama City, Pensacola, Mobile and Gulfport (Agriculture, 2021; Ashworth, 1995). However, we do not recognize subsidence in some urban districts developed upon compressible deposits, for instance, Baton Rouge, Victoria, Kingsville (Agriculture, 2021; Ashworth, 1995). It may be that subsidence over these areas was dormant or presented at rate below our identification threshold of 10 mm/year during the period of 2007–2011.

Surficial geology of the GC is complicated, consisting of a mosaic of lithofacies with Pleistocene and Holocene sediments covering most of the outcrop areas, and constituted by large amounts of unconsolidated sands, clay shales, clays and sandy clays into depth of few kilometers (Agriculture, 2021; Ashworth, 1995). The measured subsidence is generally correlated with the distribution of surficial geology along GC. Significant subsidence is more likely taking place in compressible surficial deposits, such as alluvial and lake deposits, which is also a natural process in delta system. Deltaic sediments are highly compressible and susceptible to significant natural compaction during deposition and subsequent soil formation. Land subsidence due to both nature and human activities is widely recognized over New Orleans area (Fig. 5) (Dokka, 2011). However, the magnitude of subsidence seems not fully related to the type of surface sediment unit (Fig. 6a). In Com1, we could see clear differential settlement between the buildings built before 1998 and that built after 1998, both of which are located on Harahan clay (Ha). The same differential movement also happened to Com2 on Westwego clay (Ww). Variable subsidence rates have been observed in a single type sediment. Regarding the largest subsided community in Belle Chasse, which is located on Westwego clay to the west and Schriever clay (Sk) to the east, no discontinuous phase could be observed along the boundary of distinct soil sediment units. All these indicate that the subsidence over these communities is highly correlated with the construction activities, but there is no clear evidence of the correlation between the observed subsidence and specific soil types (Fig. 6). We have also investigated other areas of subsidence that are located at contact regions along the boundary of mixed soil types, such as, sand-

dominated and clay-dominated, as well as shales-dominated and clay-dominated, and have reached the same conclusion (Agriculture, 2021). Even though the subsidence was very much influenced by the underground geology, it was not fully related to the localized surface soil units over the majority of GC. The contact regions among different soil types are usually low cohesive and would be easily developed into normal faults. For instance, the Hockley fault in Houston area lies along the contacts of the clay-dominated Willis at the upthrown fault block and the sand-dominated Lissie formations on the downthrown block of the fault (Qu et al., 2019).

In summary, the mapped subsidence along GC is consequence of combined impacts from both the regional geological conditions and the human activities. Land use changes associated with anthropogenic activities have influenced natural surroundings, and consequentially exacerbated rates of local ground subsidence. Depressurizations of petroleum reservoir are suggested to be the principal impactor on subsidence in GC sediments, secondarily to be aquifer compaction related to groundwater withdraw, other processes, including sulfur/salt mining, dewatering, oxidation, and construction work, also contributed to the InSAR-mapped subsidence patterns.

## 5. Conclusion

This paper addresses the land deformation of the GC and unveils the related geohazards by using satellite radar image processing techniques. First, we construct, for the first time, a deformation map for 500,000 km<sup>2</sup> over the Gulf Coast, spanning ~1900 km from east to west. The accuracy of the InSAR observations of deformation is 10 mm/yr based on comparison with GPS measurements. Second, the GC is generally stable except for the broad-scale subsidence caused by groundwater pumping near major metropolitan areas, such as Houston, Beaumont and New Orleans. Third, we have identified >20 localized subsidence cones over hydrocarbon exploration fields. The subsidence patterns, with spatial scales ranging from 1 to 10 km in diameter, were likely caused by reservoir compaction. Fourth, we recognize subsidence of ~60 mm/yr at The Five Islands of Louisiana. The high spatial correlation between subsidence and salt mining systems as well as the absence of oil/gas exploration activities indicate that the conventional room-and-pillar salt mining method depending on heavy machinery in the underground could be responsible for the observed subsidence. Fifth, we illustrate that the occurrence of shallow sediment compaction due to construction loading could last longer than a decade following the construction. Finally, we also realize remarkable uplifts over active disposal/injection and gas storage wells in south and east Texas, with at least 11 cones of uplift that are roughly circular in shape and typically span ~2 km in diameter. Most of the identified ground instabilities are newly discovered as a result of this study, which have been initiated by both the natural and anthropogenic processes, sometimes occurring simultaneously, including faulting, sediment compaction, hydrocarbon production, salt mining, wastewater injection, construction work, dewatering, as well as drainage and oxidation of organic soil. Our results enhance the understanding on the state of land deformation and causal mechanisms in the GC and are critically important for hazard prediction and mitigation in the region.

## CRedit authorship contribution statement

**Feifei Qu:** Methodology, Software, Formal analysis, Data curation, Writing – original draft, Writing – review & editing. **Zhong Lu:** Conceptualization, Writing – review & editing, Funding acquisition, Project administration. **Jinwoo Kim:** Formal analysis, Resources, Writing – review & editing. **Michael J. Turco:** Resources, Writing – review & editing, Funding acquisition.



## Declaration of Competing Interest

The authors declare that they have no known competing financial interests or personal relationships that could have appeared to influence the work reported in this paper.

## Data availability

Data will be made available on request.

## Acknowledgments

This research was supported by the NASA NISAR Science Team [80NSSC19K1491], NASA Surface and Interior Program [NNX16AL10G], Harris-Galveston Subsidence District, and the Shuler-Foscue Endowment at Southern Methodist University.

## Appendix A. Supplementary data

Supplementary data to this article can be found online at <https://doi.org/10.1016/j.rse.2022.113342>.

## References

- Agriculture, 2021. Web Soil Survey. Natural Resources Conservation Service, USDA.
- Ashworth, J.B., 1995. Aquifers of Texas. Texas Water Development Board, Austin, Texas.
- Autin, W.J., 2002. Landscape evolution of the five islands of South Louisiana: scientific policy and salt dome utilization and management. *Geomorphology* 47, 227–244.
- Baker, E.T.J., 1995. Stratigraphic nomenclature and geologic sections of the Gulf Coastal Plain of Texas. In: Regional Aquifer-System Analysis Program. U.S. GEOLOGICAL SURVEY, Austin, Texas, p. 28.
- Bawden, G.W., Johnson, M.R., Kasmarek, M.C., Brandt, J., Middleton, C.S., 2012. Investigation of land subsidence in the Houston-Galveston region of Texas by using the global positioning system and interferometric synthetic aperture radar, 1993–2000. In: U.S. Geological Survey Scientific Investigations Report 2012-5211, p. 88.
- Bekaert, D., Hooper, A., Wright, T., 2015. A spatially variable power law tropospheric correction technique for InSAR data. *J. Geophys. Res. Solid Earth* 120, 1345–1356.
- Berardino, P., Fornaro, G., Lanari, R., Sansosti, E., 2002. A new algorithm for surface deformation monitoring based on small baseline differential SAR interferograms. *IEEE Trans. Geosci. Remote Sens.* 40, 2375–2383.
- Blewitt, G., Hammond, W.C., Kreemer, C., 2018. Harnessing the GPS data explosion for interdisciplinary science. *EarthSci. News* 99.
- Board, T.W.D., 2020. Water Data Interactive. Texas Water Development Board.
- Bohloli, B., Bjørnarå, T.L., Park, J., Rucci, A., 2018. Can we use surface uplift data for reservoir performance monitoring? A case study from In Salah, Algeria. *Int. J. Greenhouse Gas Control* 76, 200–207.
- Brian, E., Lock, D.H.K., 2000. Salt Mines of South Louisiana: A Guidebook to Accompany Field Trip #8, April 20, 2000. 2000 AAPG Annual Convention, New Orleans.
- Buckley, S.M., Rosen, P.A., Hensley, S., Tapley, B.D., 2003. Land subsidence in Houston, Texas, measured by radar interferometry and constrained by extensometers. *J. Geophys. Res. Solid Earth* 108.
- Chaussard, E., Amelung, F., Abidin, H., Hong, S.-H., 2013. Sinking cities in Indonesia: ALOS PALSAR detects rapid subsidence due to groundwater and gas extraction. *Remote Sens. Environ.* 128, 150–161.
- Chowdhury, A.H., Turco, Mike J., 2006. Geology of the Gulf Coast Aquifer, Texas. In: Mace, Robert E., Davidson, Sarah C., Angle, A. Edward S., Mullican, I. William F. (Eds.), *Aquifers of the Gulf Coast of Texas*. Texas Water Development Board, pp. 23–50.
- Cisar, M.T., Stovall, R.M., 1998. McAllen Ranch Field: Success in the 3-D Based Redevelopment Program, Hidalgo County Texas.
- Coplin, L.S., Galloway, D., 1999. In: Houston-Galveston, Texas-Managing coastal subsidence. Land subsidence in the United States: US Geological Survey Circular, 1182, pp. 35–48.
- Drillinginfo, 2022. Drilling Info's database. <http://info.drillinginfo.com/>.
- DeLaune, R., White, J.R., 2012. Will coastal wetlands continue to sequester carbon in response to an increase in global sea level?: a case study of the rapidly subsiding Mississippi river deltaic plain. *Clim. Chang.* 110, 297–314.
- Dixon, T.H., Amelung, F., Ferretti, A., Novali, F., Rocca, F., Dokka, R., Sella, G., Kim, S.-W., Wdowinski, S., Whitman, D., 2006. Subsidence and flooding in New Orleans. *Nature* 441, 587–588.
- Dokka, R.K., 2011. The role of deep processes in late 20th century subsidence of New Orleans and coastal areas of southern Louisiana and Mississippi. <sb: contribution><sb:title>J. Geophys. Res. Solid</sb:title></sb:contribution><sb: host><sb:issue><sb:series><sb:title>Earth</sb:title></sb:series></sb: issue></sb:host> 116.
- Dokka, R.K., Sella, G.F., Dixon, T.H., 2006. Tectonic control of subsidence and southward displacement of southeast Louisiana with respect to stable North America. *Geophys. Res. Lett.* 33.
- Doornhof, D., Kristiansen, T.G., Nagel, N.B., Pattillo, P.D., Sayers, C., 2006. Compaction and subsidence. *Oilfield Rev.* 18, 50–68.
- Durrani, A., Escovedo, B., Ordemann, B., Bickley, J., Tepper, B., Simon, J., 1994. The rejuvenation of the 30-year-old McAllen Ranch. *J. Pet. Technol.* 46, 1065–1072.
- Ege, J.R., 1984. In: Survey, U.S.G. (Ed.), *Formation of Solution-Subsidence Sinkholes Above Salt Beds*. U.S. Geological Survey, Alexandria, VA.
- Ellsworth, W.L., 2013. Injection-induced earthquakes. *Science* 341.
- Ewing, T.E., Anderson, R., Babalola, O., Hubby, K., Padilla y Sanchez, R., Reed, R., 1986. Structural Styles of the Wilcox and Frio Growth-Fault Trends in Texas: Constraints on Geopressed Reservoirs. Univ. of Texas, Austin, TX (United States).
- Fattahi, H., Simons, M., Agram, P., 2017. InSAR time-series estimation of the ionospheric phase delay: and extension of the split range-spectrum technique. *IEEE Trans. Geosci. Remote Sensing* 55.
- Ferretti, A., Prati, C., Rocca, F., 2001. Permanent scatterers in SAR interferometry. *IEEE Trans. Geosci. Remote Sens.* 39, 8–20.
- Galloway, D.L., Bawden, G.W., Leake, S.A., Honegger, D.G., 2008. Land subsidence hazards. In: Baum, R.L., Galloway, D.L., Harp, E.L. (Eds.), *Landslide and Land Subsidence Hazards to Pipelines* Geological Survey (US).
- Galloway, D.L., Burbey, T.J., 2011. Regional land subsidence accompanying groundwater extraction. *Hydrogeol. J.* 19, 1459–1486.
- Galloway, D.L., Jones, D.R., Ingebritsen, S.E., 1999. Land Subsidence in the United States. US Geological Survey.
- Geoinformatics, 2019. It's Official: Louisiana Is Sinking. <https://www.lsu.edu/eng/new/s/2019/07/louisianaissinking.php>.
- Haase, C.S., Stow, S., 1988. Precise Leveling Determination of Surface Uplift Patterns at the New Hydraulic Fracturing Facility, Oak Ridge National Laboratory. Oak Ridge National Lab.
- Hamilton, D.S., 1995. Approaches to identifying reservoir heterogeneity in barrier/strandplain reservoirs and the opportunities for increased oil recovery: an example from the prolific oil-producing Jackson-Yegua trend, south Texas. *Mar. Pet. Geol.* 12, 273–290.
- Hoentzsch, S., Aubertin, J., Voigt, J., 2019. Geology of the Weeks Island Salt Dome with a focus on the current 1,500 ft. level of the Morton Salt Mine.
- Holzer, T.L., Galloway, D.L., 2005. Impacts of land subsidence caused by withdrawal of underground fluids in the United States. *Humans as geologic agents* 16, 87–99.
- Hooper, A., 2008. A multi-temporal InSAR method incorporating both persistent scatterer and small baseline approaches. *Geophys. Res. Lett.* 35, L16302.
- Hooper, A., Zebker, H., Segall, P., Kampes, B., 2004. A new method for measuring deformation on volcanoes and other natural terrains using InSAR persistent scatterers. *Geophys. Res. Lett.* 31, L23611.
- Hooper, A., Zebker, H.A., 2007. Phase unwrapping in three dimensions with application to InSAR time series. *JOSA A* 24, 2737–2747.
- Huffman Jr., A.C., Kinney Jr., S.A., Biewick Jr., L., Mitchell Jr., H.R., Gunther Jr., G.L., 2004. Gulf Coast Geology (GCG) Online–Miocene of Southern Louisiana. U.S. Geological Survey, Central Energy Resources Team, Denver, Colorado.
- HGSD, 2013. 2013 annual groundwater report. Friendswood, TX.
- HGSD, 2013. Regulatory plan 2013. Friendswood, TX.
- Jefferson, E., 1990. Evaluation of Water Resources of Orange and Eastern Jefferson Counties, Texas.
- Jones, C., Blom, R., Latini, D., 2014. Application of InSAR to detection of localized subsidence and its effects on flood protection infrastructure in the New Orleans area. In: EGU General Assembly Conference Abstracts.
- Jones, C.E., An, K., Blom, R.G., Kent, J.D., Ivins, E.R., Bekaert, D., 2016. Anthropogenic and geologic influences on subsidence in the vicinity of New Orleans, Louisiana. *J. Geophys. Res. Solid Earth* 121, 3867–3887.
- Khan, S.D., Huang, Z., Karacay, A., 2014. Study of ground subsidence in northwest Harris county using GPS, LiDAR, and InSAR techniques. *Nat. Hazards* 73, 1143–1173.
- Kim, J.-W., Lu, Z., 2018. Association between localized geohazards in West Texas and human activities, recognized by Sentinel-1A/B satellite radar imagery. *Sci. Rep.* 8, 1–13.
- Konikow, L.F., 2013. Groundwater depletion in the United States (1900–2008). US Department of the Interior. US Geological Survey Reston, Virginia.
- Konikow, L.F., 2015. Long-term groundwater depletion in the United States. *Groundwater* 53, 2–9.
- Kruger, J.M., 2019. Potential use of Subsidence Rates Determined From GPS-Based Height Modernization Measurements of NGS Benchmarks in Southeast Texas for Flood Risk Planning. In: AGU 2019. San Francisco, CA, USA. American Geophysical Union, Fall Meeting 2019, abstract #NH31E-0896.
- LPHI, A., 2016. In: Groundwater for Power Plants: A Big Risk to New Orleans East. Louisiana Public Health Institute and Alliance for Affordable Energy, p. 16.
- Lu, Z., Dzurisin, D., 2014. In: *InSAR Imaging of Aleutian Volcanoes*. Springer, pp. 87–345.
- Martin, A., Whiteman, C.D., 1999. Hydrology of the Coastal Lowlands Aquifer System in Parts of Alabama. US Department of the Interior, US Geological Survey, Florida, Louisiana, and Mississippi.
- Martinez, J.D., 1991. Salt domes. *Am. Sci.* 79, 13.
- McGarr, A., Bekins, B., Burkardt, N., Dewey, J., Earle, P., Ellsworth, W., Ge, S., Hickman, S., Holland, A., Majer, E., 2015. Coping with earthquakes induced by fluid injection. *Science* 347, 830–831.
- Miller, J.A., 1999. Ground water atlas of the United States: Introduction and national summary. In: US Geological Survey.
- Miller, M.M., Shirzaei, M., 2019. Land subsidence in Houston correlated with flooding from Hurricane Harvey. *Remote Sens. Environ.* 225, 368–378.
- Morton, R.A., 2003. An overview of coastal land loss: with emphasis on the Southeastern United States. In: U.S. Geological Survey Open File Report 03-337, p. 24.

- Morton, R.A., Bernier, J.C., Barras, J.A., 2006. Evidence of regional subsidence and associated interior wetland loss induced by hydrocarbon production, Gulf Coast region, USA. *Environ. Geol.* 50, 261.
- Morton, R.A., Paine, J.G., Robinson, D., 1983. Historical Monitoring of Shoreline Changes in Corpus Christi, Nueces, and Oso Bays. Bureau of Economic Geology, University of Texas at Austin.
- Neal, J.T., Magorian, T., Thoms, R., Autin, W., McCulloh, R., Denzler, S., Byrne, K., 1993. Anomalous Zones in Gulf Coast Salt Domes with Special Reference to Big Hill, TX, and Weeks Island, LA. Sandia National Labs, Albuquerque, NM (United States).
- Paine, J.G., 1993. Subsidence of the Texas coast: inferences from historical and late Pleistocene sea levels. *Tectonophysics* 222, 445–458.
- Qu, F., Lu, Z., Kim, J.-W., Zheng, W., 2019. Identify and monitor growth faulting using InSAR over Northern Greater Houston, Texas, USA. *Remote Sens.* 11, 1498.
- Qu, F., Lu, Z., Zhang, Q., Bawden, G.W., Kim, J.-W., Zhao, C., Qu, W., 2015. Mapping ground deformation over Houston-Galveston, Texas using multi-temporal InSAR. *Remote Sens. Environ.* 169, 290–306.
- Qu, F., Zhang, Q., Lu, Z., Zhao, C., Yang, C., Zhang, J., 2014. Land subsidence and ground fissures in Xi'an, China 2005–2012 revealed by multi-band InSAR time-series analysis. *Remote Sens. Environ.* 155, 366–376.
- Ratzlaff, K.W., 1980. Land-surface subsidence in the Texas coastal region. In: US Geological Survey.
- Rogers, J.D., Boutwell, G., Watkins, C., Karadeniz, D., 2006. Chapter Three: Geology of the New Orleans Region.
- Seifert, J., Drabek, C., 2006. History of production and potential future production of the Gulf Coast Aquifer. In: Mace, R.E., Davidson, S.C., Angle, E.S., Mullican III, W.F. (Eds.), *Aquifers of the Gulf Coast of Texas*. Texas Water Development Board Report, pp. 261–271.
- Shirzaei, M., Ellsworth, W.L., Tiampo, K.F., González, P.J., Manga, M., 2016. Surface uplift and time-dependent seismic hazard due to fluid injection in eastern Texas. *Science* 353, 1416–1419.
- Shirzaei, M., Manga, M., Zhai, G., 2019. Hydraulic properties of injection formations constrained by surface deformation. *Earth Planet. Sci. Lett.* 515, 125–134.
- Sneed, M.I., Marti, E., Stork, V., Stork, Amelung, Falk, Galloway, Devin L., 2003. Detection and measurement of land subsidence using interferometric synthetic aperture radar and global positioning system, San Bernardino County, Mojave Desert, California [J.], 2003, 3: 4015. In: *Water-Resources Investigations Report 03-4015*. Sacramento, California: U.S. GEOLOGICAL SURVEY.
- Snowden, J.O., Simmons, W.B., Traughber, E.B., Stephens, R.W., 1977. Differential subsidence of marshland peat as a geologic hazard in the greater New Orleans area, Louisiana.
- Stork, S.V.S., Michelle, 2002. Houston-Galveston Bay area, Texas, from Space-a new tool for mapping land subsidence. In: US Geological Survey Fact Sheet 110.
- Stuart, C.A., 1970. Geopressures. Shell Oil Company, New Orleans, LA.
- Swanson, R., Oetking, P., Osoba, J., Hagens, R., 1976. Development of an Assessment Methodology for Geopressured Zones of the Upper Gulf Coast Based on a Study of Abnormally Pressured Gas Fields in South Texas. Energy Research and Development Administration, Washington, DC (USA). Div.
- Swanson, S.M., Karlsen, A.W., Warwick, P.D., 2007. USGS Assessment of Undiscovered Oil and Gas Resources for the Oligocene Frio and Anahuac Formations, US Gulf of Mexico Coastal Plain and State Waters: Review of Assessment Units.
- Texas Water Development Board, 2020. Water data interactiv. <https://www.twdb.texas.gov/mapping/>.
- Texas, 2020. Maps - Public GIS Viewers, Texas RRC, RRC. <https://www.rrc.texas.gov/media/xyhpsfk/gsd-gas-storage-report-072021.pdf>.
- Van der Baan, M., Calixto, F.J., 2017. Human-induced seismicity and large-scale hydrocarbon production in the USA and Canada. *Geochim. Geophys. Res.* 18, 2467–2485.
- Wang, F.P., Loucks, Robert G., 2002. In: Effect of Hydrocarbon Production and Depressurization on Subsidence and Possible Fault Reactivation: Port Arches- Port Arthur Filed Area, Southeast Texas. Bureau of Economic Geology & The University of Texas at Austin, Austin, Texas, p. 26.
- Wang, G., Turco, M., Soler, T., Kearns, T.J., Welch, J., 2017. Comparisons of OPUS and PPP solutions for subsidence monitoring in the greater Houston area. *J. Surv. Eng.* 143, 05017005.
- Wegmüller, U., Werner, C., Frey, O., Magnard, C., Strozzi, T., 2018. Reformulating the split-spectrum method to facilitate the estimation and compensation of the ionospheric phase in SAR interferograms. *Proc. Comput. Sci.* 138, 318–325.
- Wintz, W.A., Kazmann, R.G., Smith, C.G., 1970. Subsidence and groundwater offtake in the Baton Rouge area.
- Wright, T., Parsons, B., Fielding, E., 2001. Measurement of interseismic strain accumulation across the North Anatolian Fault by satellite radar interferometry. *Geophys. Res. Lett.* 28, 2117–2120.
- Yu, C., Li, Z., Penna, N.T., Crippa, P., 2018. Generic atmospheric correction model for Interferometric Synthetic Aperture Radar observations. *J. Geophys. Res. Solid Earth* 123, 9202–9222.
- Zebker, H.A., Villasenor, J., 1992. Decorrelation in interferometric radar echoes. *IEEE Trans. Geosci. Remote Sens.* 30, 950–959.
- Zhou, X., Wang, G., Wang, K., Liu, H., Lyu, H., Turco, M.J., 2021. Rates of natural subsidence along the Texas coast derived from GPS and Tide Gauge Measurements (1904–2020). *J. Surv. Eng.* 147, 04021020.